Generation and Detection of Optical Beams with Orbital Angular Momentum using a Spatial Light Modulator

Kimberly Kurzbach

Bachelorarbeit in Physik
angefertigt im Institut für Angewandte Physik

vorgelegt der
Mathematisch-Naturwissenschaftlichen Fakultät
der
Rheinischen Friedrich-Wilhelms-Universität
Bonn

Mai 2024

Ich versichere, dass ich diese Arbeit selbstständig verfasst und keine anderen als die angegebenen Quellen und Hilfsmittel benutzt sowie die Zitate kenntlich gemacht habe.

Bonn, 07.05.2024 Kurzbach

Datum Unterschrift

1. Gutachter: Prof. Dr. Sebastian Hofferberth
2. Gutachter: Prof. Dr. Stefan Linden

Contents

CHAPTER 1

Introduction

In the past 100 years, the knowledge about atoms has increased enormously, from the first observations of atomic spectra with discharge lambs to the discovery and theoretical understanding of the couplings between different angular momenta that leads to fine and hyperfine atomic structure.

The demonstration of atom-trapping and cooling in the 1980s [1] and the following breakthroughs such as the first Bose-Einstein condensation in 1995 [2] allowed a new level of control over atoms, and the option to probe atomic structure precisely. This includes probing the interaction between ultracold atoms and photons with orbital angular momentum (OAM). In the last three decades the investigation of the interaction between atoms and light with OAM has gained huge interest because it holds a promise for a deeper understanding of matter-light interactions and allows various applications in quantum memories and other quantum technologies such as cold-atom trapping techniques and optical tweezers [3].

The Rubidium Quantum Optics-project (RQO) at the University of Bonn explores how to manipulate single photons by sending them through a quantum-nonlinear medium created with ultracold Rydberg atoms. In general, Rydberg quantum optics relies on the strong interactions between Rydberg atoms that can be mapped onto otherwise non-interacting photons [4].

In the RQO experiment, such a nonlinear medium is realized by laser-cooling and trapping Rubidium atoms first with a magneto-optical trap (MOT) and then a large dipole trap where the atomic cloud is cooled to temperatures below 4 μK. The current aim of the experiment is the creation of multiple Rydberg superatoms. A Rydberg superatom is an ensemble of atoms as well within the Rydberg blockade radius, such that all atoms can share only a single excitation [5]. A future idea for this experiment is to investigate how Rydberg-mediated interactions between photons propagating in the ultracold gas lead to changes in the outgoing light mode. In the current experiment the Rydberg atoms are probed with few-photon pulses in a Gaussian mode. The Gaussian mode is collected with a single mode fiber. So far, this approach enables us to send the excitation photons and collect the emitted ones from the cloud only for a certain wave vector $\vec{k}$ defined by the Gaussian mode. A next step in the experiment is to collect light from more different modes, to detect whether the Rydberg-Rydberg interactions give orbital angular momentum to propagating photons, and in an even further step to probe the atoms with OAM light and observe changes.

OAM light can be created and detected in different ways, such as with phase plates as it has been

demonstrated in a different institute of the University of Bonn by A. Faßbender, S. Linden et al., where a metasurface phase plate was used to generate different Laguerre-Gaussian (LG) modes and a common-part interferometer is utilized to determine the OAM [6], with optical cavities [7], and with dynamically changeable phase or amplitude patterns created with for instance spatial light modulators (SLMs) or digital micromirror devices [8]. In this thesis, SLMs will be considered.

For the planned experiments, an SLM after the atomic cloud will be used to collect light with different OAM, and an SLM before the atoms will be used to prepare the probe pulses in modes with OAM.

In this Bachelor thesis, a SLM will be used to create OAM modes of arbitrary order. This thesis is structured as follows: First, a general introduction into optical beam profiles will be given in chapter 2. Starting by the consideration of Maxwell's equations, which form the foundation of classical electromagnetism, different solutions are derived that represent various beam profiles. Those profiles will be visualized and their OAM will be further discussed. In chapter 3 the SLM, on which the already discussed beam profiles will be later implemented on a phase-only hologram, will be introduced and its working principle as well as its image creation will be explained. The device is also going to be characterized, and a closer look is especially taken towards its phase modulation. Finally, in chapter 4 it is explored how one can create the phase masks used for the SLM, a possible setup to generate OAM beams will be shown, and their detection is going to be discussed. Additionally, possible optimization methods will be presented as well as their experimental results. To conclude, the experimental data is compared to the theoretical outcome, which is derived in the beginning.

CHAPTER 2

Insights into various Optical Beam Profiles

To comprehend how different phase holograms can be created, one has to first understand the fundamental properties of various types of optical beams. The aim of this chapter is to provide a theoretical overview of these beams, to emphasize their unique characteristics, and to mention both their differences as well as their similarities. By investigating the intricacies of Gaussian, Hermite-Gaussian and Laguerre-Gaussian beams, the reader can gain a deeper insight into their behavior and applications within the field of optics.

First, the function of a Gaussian beam will be derived from the wave and the Helmholtz equation. Further the intensity profile as well as other properties for example the waist of a Gaussian beam are going to be discussed. Then an overview of Hermite-Gaussian modes is given, and its derivation is mentioned. Furthermore, the Laguerre-Gaussian modes will also be discussed and important associations such as the optical vortex and orbital angular momentum will be explained.

2.1 Optical waves

Starting by considering an electromagnetic wave, which propagates in z-direction, the microscopic Maxwell equations in free space lead to the function of a complex scalar field U [9]

$$\nabla^2 U - \frac{1}{c^2}\frac{\partial^2 U}{\partial t^2} = 0\,, \tag{2.1}$$

where ∇ describes the Laplacian operator, c is the speed of light in free space and t represents the time. Any function that satisfies this equation can describe a possible optical wave. Using the method of separation of variables the field distribution can be expressed as a part, which only depends on the spatial variable $\vec{r}$ and one part that is only dependent on the time $U(\vec{r},t) = U(\vec{r})\exp(i\omega t)$ [10]. Here the term $U(\vec{r})$ denotes the complex amplitude of the wave, $\vec{r} = (x, y, z)$ characterizes its position and the factor ω describes its frequency.

Substituting the expression for $U(\vec{r},t)$ into Equation 2.1, will lead to the time-independent Helmholtz equation [11]

$$\nabla^2 U + k^2 U = 0\,, \tag{2.2}$$

where $k = \frac{2\pi}{\lambda}$ represents the wave number and λ denotes the wavelength.

This equation can be further approximated in the paraxial regime, which represents the limit of small angles from the optical axis [12]. Therefore, the complex envelope $A(\vec{r})$ of the wave is modulated to be a slowly varying function of its position and the complex amplitude can be written in terms of it [10]

$$U(\vec{r}) = A(\vec{r}) \exp(-ikz) \ . \tag{2.3}$$

This also implies that the change of the function $A(\vec{r})$ within the distance of a wavelength $\Delta z = \lambda$ must be smaller than A itself. Considering this assumption, it can be shown that the second derivative is way smaller than $\frac{\partial^2 A}{\partial z^2} << k^2 A$, and therefore we are able to neglect it while substituting Equation 2.3 into Equation 2.1. This leads to the paraxial Helmholtz equation [10]

$$\nabla^2 A - i2k\frac{\partial A}{\partial z} = 0 \ . \tag{2.4}$$

2.2 Gaussian beam

A Gaussian beam is characterized by an amplitude envelope represented by a Gaussian function, which arises as one of the first solutions of the paraxial Helmholtz equation. Its essential transverse electromagnetic mode TEM_{00} describes the output of a laser.
To obtain such a beam, we can consider a paraboloidal wave with a transformation of the z coordinate. Because the complex envelope represents a solution of the Helmholtz equation, it can be assumed that a shifted version of it is a solution as well. If the coordinate is set to $z \rightarrow z - \xi$ with ξ being an imaginary constant, it will lead to the function of the complex envelope [10]

$$A(\vec{r}) = \frac{A_1}{q(z)} \exp\left(-ik\frac{\rho^2}{zq(z)}\right) \ . \tag{2.5}$$

Here the factor A_1 is a constant, $q(z) = z + iz_\mathrm{R}$ is called the q-parameter and z_R is taken to be the Rayleigh range. In polar coordinates, the variable ρ is defined as the Euclidean distance from the origin, given by $\rho = \sqrt{x^2 + y^2}$.

The next step is to separate the amplitude and the phase of the complex envelope. For that, $q(z)$ is represented in terms of two functions $W(z)$ and $R(z)$, which represent the beam's width and the radius of curvature of the wavefront [10]

$$\frac{1}{q(z)} = \frac{1}{R(z)} - i\frac{\lambda}{\pi W^2(z)} \ . \tag{2.6}$$

Using this substitution of $q(z)$ in Equation 2.3 leads to the complex amplitude of a Gaussian beam [10]

$$U(\vec{r}) = A_0 \frac{W_0}{W(z)} \exp\left(-\frac{\rho^2}{W^2(z)}\right) \exp\left(-ikz - ik\frac{\rho^2}{2R(z)} + i\zeta(z)\right) \ . \tag{2.7}$$

In this equation a new constant is assumed $A_0 = \frac{A_1}{iz_R}$ and the following functions for the different beam parameters are used:

$$W(z) = W_0\sqrt{1 + \left(\frac{z}{z_R}\right)^2}\ ,\ W_0 = \sqrt{\frac{\lambda z_0}{\pi}}\ , \tag{2.8}$$

$$R(z) = z\left(1 + \left(\frac{z_R}{z}\right)^2\right)\ , \tag{2.9}$$

$$\zeta(z) = \arctan\left(\frac{z}{z_R}\right)\ . \tag{2.10}$$

The parameter z_0 characterizes the point at which the intensity distribution attains half of its peak value along the z-axis. Equation 2.10 represents the phase retardation of a Gaussian beam, which is known as the Gouy effect [10]. As z tends towards negative infinity, it converges towards $-\frac{\pi}{2}$, and as z becomes significantly large, it approaches $+\frac{\pi}{2}$, which means that a total phase retardation of π can be observed in relation to a plane or spherical wave.

2.2.1 Intensity profile

We obtain the intensity distribution from $I(\vec{r}) = |U(\vec{r})|^2$. Using this on the function of the complex amplitude of a Gaussian beam yields the intensity function

$$I(\rho, z) = I_0\left(\frac{W_0}{W(z)}\right)^2 \exp\left(-\frac{2\rho^2}{W^2(z)}\right)\ , \tag{2.11}$$

where a new constant is given by $I_0 = |A_0|^2$, which represents the maximum intensity.

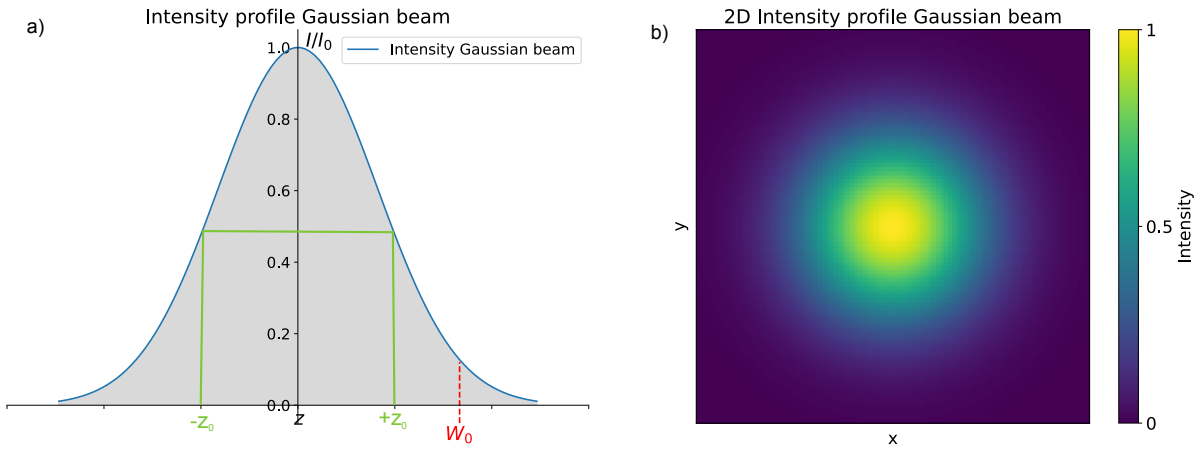

Figure 2.1: a) one dimensional Intensity profile of a Gaussian beam with the waist size W_0 and its reaching half of its maximum value at the distance $z = \pm z_0$ b) two-dimensional Intensity profile of Gaussian beam

In Figure 2.1 the intensity profile of a Gaussian beam is shown. It reaches maximum intensity in the

center, and decreases fast for an arbitrary distance. It attains half of its peak at the distance $z = \pm z_0$.

Furthermore, it can be shown that approximately 86% of the beam's intensity is contained in a circle of the radius $\rho = W(z)$. This value is obtained as the intensity decreases to $1/e^2$ of its maximum value. In conclusion, $W(z)$ can be considered the beam's radius and its function is given in Equation 2.8. W_0 can be denoted as the beam's waist, which represents the minimum value of the beam's width at $z = 0$ as shown in Figure 2.2. For the beam imaging process performed in this thesis, the waist size of the beams play an important role.

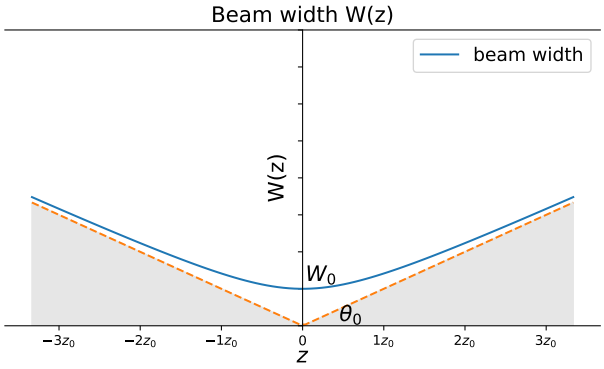

Figure 2.2: Beam width $W(z)$ of a Gaussian beam with the waist W_0 and θ_0 as the angle of divergence

For $z \gg z_0$ we are able to approximate the relation of $W(z)$ to

$$W(z) \approx \frac{W_0}{z_0} z = \theta_0 z \,, \tag{2.12}$$

where θ_0 represents the beam's angle of divergence, which we can also express as

$$\theta_0 \approx \frac{2\lambda}{\pi W_0} \,. \tag{2.13}$$

It can be seen that the beam's divergence will decrease while the waist is increasing.
Taking Equation 2.9 into account, which represents the radius of curvature of the wavefront depending on the position z, it can be noticed that the wave fronts are planar at the center ($z = 0$). However, the curvature of the wavefront increases with z and is considered equal to the wave fronts of a spherical wave.

2.3 Hermite Gaussian Modes

As already discussed, the function of the Gaussian beam is a solution of the paraxial Helmholtz equation. Other solutions of this equation are the Hermite Gaussian (HG) modes. Their amplitude function satisfies the Helmholtz equation in Cartesian coordinates.

We can modify the function of the complex envelope $A(x, y, z)$ derived in Equation 2.3 for the case of

an additional wave [10]

$$A(x,y,z) = \mathcal{X}\left(\sqrt{2}\frac{x}{W(z)}\right)\mathcal{Y}\left(\sqrt{2}\frac{y}{W(z)}\right)\exp\left(i\mathcal{Z}\right)A_{\mathrm{G}}(x,y,z)\,, \tag{2.14}$$

where A_{G} is the complex envelope of a Gaussian function and $\mathcal{X}$, $\mathcal{Y}$ and $\mathcal{Z}$ are real functions. It can be shown that those three functions satisfy the Helmholtz equation as well and by separation of variables an eigenvalue problem with the eigenvalues $n = 0, 1, 2, \ldots$ in x-direction and $m = 0, 1, 2, \ldots$ in y-direction is obtained. The eigenfunctions of those eigenvalues are the Hermite polynomials, defined as [13]

$$\mathcal{H}_n = (-1)^n \mathrm{e}^{x^2}\frac{d^n}{dx^n}\mathrm{e}^{-x^2}\,. \tag{2.15}$$

The same relation applies to the eigenfunctions of m. The Hermite polynomials are equal to the functions assumed earlier in this section and therefore $\mathcal{X}(x) = \mathcal{H}_{\mathrm{n}}(x)$ and $\mathcal{Y}(y) = \mathcal{H}_{\mathrm{m}}(y)$. Hence, we are able to show that $\mathcal{Z}(z) = (n+m)\zeta(z)$, while $\zeta(z)$ is given in Equation 2.10 as the Gouy phase. Similar to the calculations above an additional phase is obtained, which varies slowly between $-(n+m)\frac{\pi}{2}$ as z emerges towards negative infinity and $+(n+m)\frac{\pi}{2}$ for large values of z. The complex amplitude of HG beams arises from Equation 2.14 if the functions, that were implied above, are substituted and the equation is multiplied with a factor of $\exp(-ikz)$ [10]

$$\begin{aligned} U_{\mathrm{nm}}(x,y,z) = C_{\mathrm{nm}}\cdot\frac{W_0}{W(z)}\cdot\mathcal{H}_n\left(\frac{\sqrt{2}x}{W(z)}\right)\cdot\mathcal{H}_m\left(\frac{\sqrt{2}y}{W(z)}\right)\cdot\exp\left(-\frac{x^2+y^2}{W^2(z)}\right) \\ \cdot\exp\left[-ikz - ik\frac{x^2+y^2}{2R(z)} + i(n+m+1)\zeta(z)\right]\,. \end{aligned} \tag{2.16}$$

The normalization constant, which is used to obtain orthonormality, is given by [14]

$$C_{\mathrm{nm}} = \sqrt{\frac{2}{\pi\cdot 2^{(n+m)}\cdot n!\cdot m!}}\,. \tag{2.17}$$

For a wave propagating in z direction the intensity profile (at the plane $z = 0$) for different modes is obtained from [15]

$$I_{\mathrm{nm}}(x,y) = \left|U_{\mathrm{nm}}(x,y,0)\right|^2 = \left|C_{\mathrm{nm}}\cdot\mathcal{H}_{\mathrm{n}}\left(\frac{\sqrt{2}x}{W_0}\right)\cdot\mathcal{H}_{\mathrm{m}}\left(\frac{\sqrt{2}y}{W_0}\right)\cdot\exp\left(-\frac{x^2+y^2}{W_0^2}\right)\right|^2\,. \tag{2.18}$$

This leads to the intensity profile of the HG modes shown in Figure 2.3. It becomes clear that the mode HG_{00} is equivalent to the intensity distribution of a Gaussian beam (see subsection 2.2.1) and is the only mode which is circularly symmetric.

2.4 Laguerre Gaussian Modes

Another solution of the paraxial Helmholtz equation apart from the Hermite Gaussian modes is represented by the Laguerre Gaussian (LG) modes. In contrast to the derivation for the HG beams,

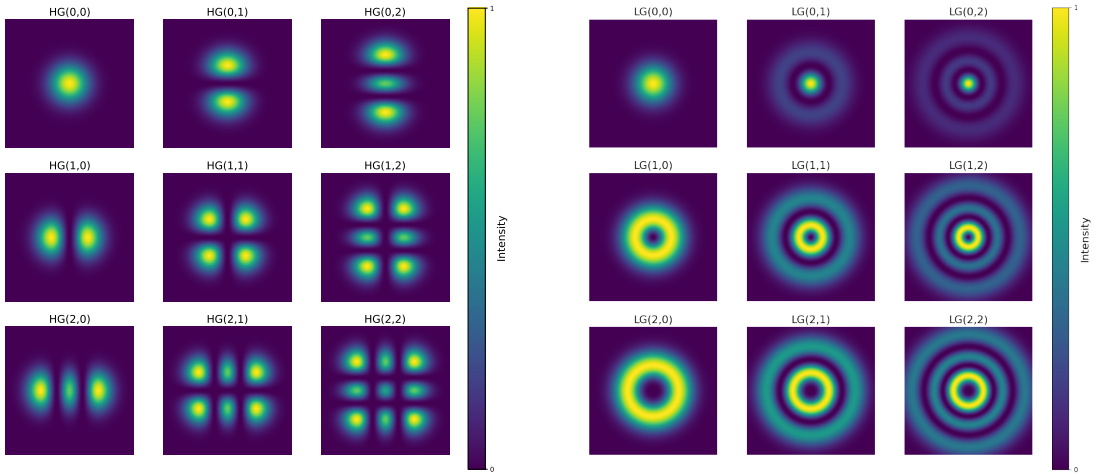

Figure 2.3: Amplitude function of different Hermite Gaussian modes HG(n,m) (left) and Laguerre Gaussian modes LG(l,p) (right)

cylindrical coordinates (ρ, ϕ, z) are considered instead of Cartesian coordinates, where the azimuth angle is defined as $\phi = \arctan\left(\frac{y}{x}\right)$. This leads to a complex amplitude of [10]

$$\begin{aligned} U_{\mathrm{lp}}(\rho,\phi,z) =& C_{\mathrm{lp}} \frac{W_0}{W(z)} \left(\frac{\rho}{W(z)}\right)^{|l|} L_{\mathrm{p}}^{(\mathrm{l})}\left(\frac{2\rho^2}{W^2(z)}\right) \exp\left(-\frac{\rho^2}{W^2(z)}\right) \\ & \cdot \exp\left[-ikz - ik\frac{\rho^2}{2R(z)} - il\phi + i(l+2p+1)\zeta(z)\right] . \end{aligned} \tag{2.19}$$

The normalization constant is given by [16]

$$C_{\mathrm{lp}} = \sqrt{\frac{2p!}{\pi(p+\mid l \mid)!}} . \tag{2.20}$$

The eigenvalue l represents the azimuthal index and can be positive, negative or equal to zero while the eigenvalue p describes the radial index, which must be greater or equal to zero. Furthermore, the eigenfunctions are given by the generalized Laguerre polynomials, which are defined by the Rodrigues formula [13]

$$L_{\mathrm{p}}^{(\mathrm{l})}(x) = \frac{x^{-l}\mathrm{e}^{x}}{p!}\left(\frac{d^p}{dx^p}\right)\left(x^{l+p}\mathrm{e}^{-x}\right) . \tag{2.21}$$

Moreover, it also becomes obvious that the Gouy phase for LG beams includes an additional factor of $(l + 2p + 1)$ resulting in a greater value of the total phase retardation compared to that one of a Gaussian or HG beam for a specific mode.

In addition, the intensity profile (at the plane $z = 0$) can be derived as [15]

$$I_{\mathrm{lp}}(\rho,\phi) = |U(\rho,\phi,0)|^2 = \left| C_{\mathrm{lp}} \cdot \left(\frac{\sqrt{2}\rho}{W_0}\right)^{|l|} \cdot L_{\mathrm{p}}^{(1)} \cdot \exp\left(-\frac{\rho^2}{W_0^2}\right) \cdot \exp(il\phi) \right|^2 . \tag{2.22}$$

For the LG_{00} mode, the intensity distribution of a Gaussian beam is obtained, as shown in Figure 2.3. The rest of the modes shown here also indicate a circular symmetry. This is a result of the dependency of the phase on ρ, which is equivalent to a Gaussian beam (see Equation 2.7). But another term has to be considered for LG beams, which is dependent on the angle ϕ as seen in Equation 2.19. Thus, a helically tilt in the wavefront is observed as the wave travels through space. This can be described by the concept of an optical vortex and is of great interest because such beams carry orbital angular momentum (OAM), which is able to add torque to the photon [17]. If l is greater than zero, the beam will have no intensity at the center and an optical vortex can be identified. Next section follows with the discussion of this phenomena.

2.4.1 Optical vortex and OAM of light

The concept of an optical vortex describes points in the intensity distribution of a light beam which are equal to zero. Those points are also called singularities, that denote places where mathematical or physical quantities become infinite or change abruptly [18]. The phase of the electromagnetic field revolves around those points of zero intensity.

An optical vortex is characterized by a number, called the topological charge. The topological charge is equal to the number of twists that are encountered within one wavelength. For LG beams the topological charge is equal to the azimuthal index l.

As already discussed in section 2.4, as some light beams travel through space, they exhibit rotation. Hence, they carry angular momentum, which will result in either spin, if every polarization vector rotates or OAM, if every phase structure rotates, which can be much greater than the spin [17]. If a light beam contains an azimuthal phase dependency of $\exp(il\phi)$, they will carry OAM. The wavefront is shaped like a helix (helical phase distribution) and an optical vortex is formed in the center, while both the number of intertwined helices and the handedness of the phase depend on the value and the sign of the topological charge l [17].

The helical phase of a wave, which carries OAM is shown in Figure 2.4. The wavefront is shaped like a helix and a vortex can be seen at the center. The figure shows that we cannot observe a helical mode for $l = 0$. For $l = \pm 1$ the shape of a single helix is displayed and a vortex can be identified. Furthermore, the wavefront for values of $l = \pm 2$ or larger is composed of l intertwined helices [19].

The most common function Ψ featuring a phase singularity is the mapping from Cartesian coordinates to the complex domain

$$\Psi(x,y) = x + iy = \rho\exp(i\phi) = \rho\exp\left(i\arctan\left(\frac{y}{x}\right)\right) , \tag{2.23}$$

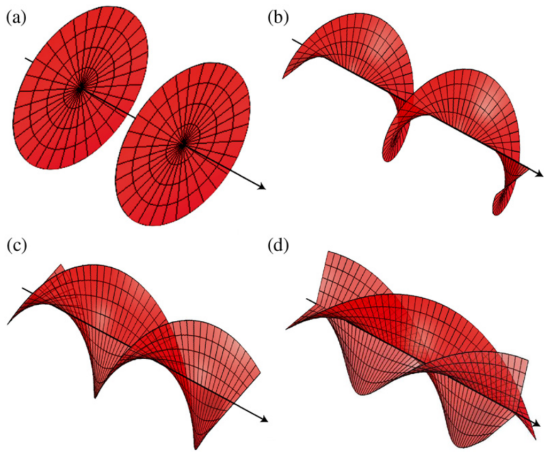

Figure 2.4: Helical phase fronts for (a) $l = 0$ (b) $l = 1$, (c) $l = 2$ and (d) $l = 3$ (taken from [17])

where $\rho = \sqrt{x^2 + y^2}$ denotes the Euclidean distance and $\phi = \arctan\left(\frac{y}{x}\right)$ is the polar angle, which is not defined at the center but everywhere else. A singularity can be observed at the center of the coordinate system $(x = y = 0)$.

One needs to emphasize that the optical vortex in the center carries no energy and therefore no angular momentum, which implies that the origin of OAM lies not within the singularity itself but in the light surrounding it. The value of the OAM is equivalent to $l\hbar$ per photon and therefore is quantized in terms of $\hbar$ just like the spin with the difference that it is independent of the polarization state of the beam [20].

CHAPTER 3

Principles and Operations of Spatial Light Modulators

So far, the properties of different beams have been discussed separately, but it is possible to transform one type of beam, for instance a Gaussian beam, into another, for example a LG beam. To do this, one needs to modify the phase or amplitude of the original beam such that the new beam has the desired properties. In practice, this can be done, for instance by passing the beam through a phase mask. Spiral phase plates with one specific phase pattern can be bought from optics suppliers [21]. It is also possible to create changeable phase patterns with devices like a digital micrometer (DMD), which contains several hundred thousand microscopic mirrors that correspond to a different pixel value by rotation of its alignment [8]. In this thesis, phase patterns are created with an SLM and therefore the device will be further discussed in this chapter.

First, we discuss a principle scheme of SLM operation. Then, we take the mathematical aspect into account and take a look at the Fresnel as well as the Fraunhofer approximation to show that a thin lens can be used to perform a Fourier transform of the reflected light by the SLM. After that we will take a closer look at the specific SLM, that is used in this thesis. The phase modulation of the device is checked and compared for different settings. The polarization of this setup will also be discussed and visualized. Finally, different gratings are tried out and therefore we can measure the diffraction efficiency.

3.1 Fundamentals of Spatial Light Modulators (SLM)

A spatial light modulator (SLM) is a device, which is able to either modulate the amplitude or the phase (or both) of the incident light [22]. In this thesis a phase-only modulating device is used, specifically a liquid crystal on silicon (LCOS) SLM, which works in reflection.

A liquid crystal (LC) is placed between a glass substrate and a CMOS (complementary metal oxide semiconductor) chip, in which multiple pixel electrodes are positioned in a two-dimensional array [23]. The structure of the different layers used in a SLM can be seen in Figure 3.1. Liquid crystals are considered to be materials, which exhibit properties between the ones of solids and liquids [22]. The LC molecules both show electrical as well as optical anisotropies. The electrical anisotropy leads to a dipole behavior of the LC and the optical anisotropy induces birefringence, which results in different

refractive indices n for different LC molecules [24]. The phase velocity $v = \frac{c}{n}$ is dependent on the index of refraction. Therefore, the phase of the reflected wave can be modulated, if the index of refraction is spatially varied [25]. If an electric field is applied across this layer, the electrical anisotropy will produce a certain tilt of the LC molecules. Because of the optical anisotropy the tilt will change the refractive index of the molecules. In addition, the light propagates faster in regions with a larger tilt and hence the wavefront of the light changes when being reflected on the surface.

To create an image that can be used on the SLM the phase values, which lie in the range of $[0, 2\pi]$, need to be converted to numerical values in the range of for example [0,255] (8 bit). Those values are then converted into a bit mapped image with the same resolution as the SLM. Each gray level of the bit mapped image represents a different input signal level, which implies a certain voltage to a LC molecule. Because of the different voltages, the LC molecules will experience a different tilt.

To obtain the best phase shifts, the polarization of an incident beam must be well-aligned with the orientation of the LC molecules. This orientation is set by two transparent alignment films that are placed on the sides of the LC layer. The LC molecules in the SLM used here appear to be orientated horizontally (when the SLM is mounted with a post to the optical table). Therefore, the SLM is only intended to be used with horizontally polarized light. The transparent electrode on top is used of to apply the already mentioned electric field [25].

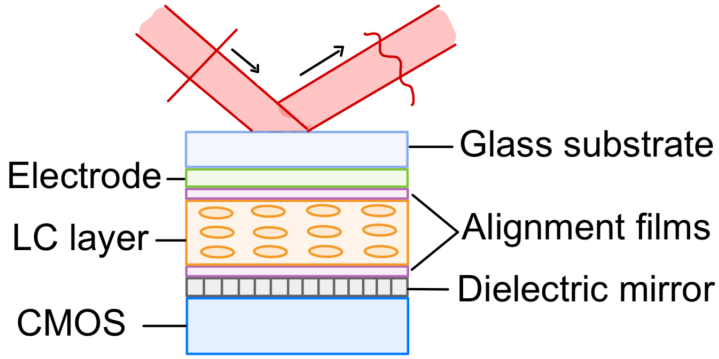

Figure 3.1: Configuration of LCOS-SLM where a liquid crystal is placed between glass substrate and a CMOS. The dielectric mirror is used to increase the efficiency of the used light. The digital image uploaded to the SLM is converted to an analog signal, which applies a voltage to the pixels of the CMOS chip [23].

3.2 Image projection using a Fourier transform

The previous section introduced the working principle of a SLM for creating changeable phase patterns. This section will discuss how phase patterns displayed onto the SLM influence the intensity patterns that can be detected on, for instance a camera.

The Huygens-Fresnel principle [11, 25] implies that each point on the wavefront of an electromagnetic wave serves as the origin of a second wave package. If a wave propagates in z direction through an aperture with the complex amplitude $U(\xi, \eta)$, the field at the observation point P_O can be expressed as the following

$$U(P_\mathrm{O}) = \int \int_S U(P_\mathrm{A}) \frac{\mathrm{e}^{ikr}}{r} \psi(\theta) ds \,, \tag{3.1}$$

where S represents the aperture and r characterizes the distance between the point of observation P_O and the point of aperture P_A. The geometry of the diffraction is visualized in Figure A.1. The angle θ denotes the angle between the normal of the aperture and the vector r, which is pointing from the point of the aperture to the point of observation. The factor $\psi(\theta)$ was implied by Fresnel, considering the amplitude and the phase of the secondary wavelet. Later, it was shown by Kirchhoff that this factor is equivalent to $\psi(\theta) = \cos(\theta) = \frac{z}{r}$ [25].

Equation 3.1 can also be written in Cartesian coordinates [11]

$$U(x, y) = \frac{z}{i\lambda} \int \int_S U(\xi, \eta) \frac{\mathrm{e}^{ikr}}{r^2} d\xi d\eta \,, \tag{3.2}$$

where the vector r can be also expressed as the following

$$r = z \sqrt{1 + \left(\frac{x - \xi}{z}\right)^2 + \left(\frac{y - \eta}{z}\right)^2} \,. \tag{3.3}$$

The Fresnel approximation, which can also be considered to represent the near field of the distribution, yields

$$r \approx z \left[1 + \frac{1}{2} \left(\frac{x - \xi}{z}\right)^2 + \left(\frac{y - \eta}{z}\right)^2\right] \,. \tag{3.4}$$

Therefore, the complex amplitude in Fresnel approximation can be written as [11]

$$U(x, y) = \frac{\mathrm{e}^{ikz}}{i\lambda z} \mathrm{e}^{i\frac{k}{2z}(x^2+y^2)} \int \int_{-\infty}^{\infty} \left[U(\xi, \eta) \mathrm{e}^{i\frac{k}{2z}(\xi^2+\eta^2)}\right] \mathrm{e}^{-\frac{ik}{z}(x\xi+y\eta)} d\xi d\eta \,. \tag{3.5}$$

This equation is called the Fresnel diffraction integral and is equivalent to a Fourier transform of the complex field (right next to the aperture) multiplied by a quadratic phase exponential term. Here the paraxial approximation holds.

On the other hand, there is also the Fraunhofer approximation, which is equal to considering the far field of the distribution. In principle, the terms far field and near field are known from classical electromagnetism. The near field is characterized close to the object where the radiation is emitted, and the far field denotes the region far away, where the electromagnetic radiation is dominated by electric dipole characteristics [26]. Therefore, the term for r in Equation 3.3 can also be estimated in Fraunhofer approximation and be rewritten as

$$z \gg \frac{k(\xi^2 + \eta^2)}{2} \,, \tag{3.6}$$

which leads to a complex amplitude of [11]

$$U(x,y) = \frac{e^{ikz}}{i\lambda z} e^{i\frac{k}{2z}(x^2+y^2)} \int\int_{-\infty}^{\infty} U(\xi,\eta) e^{\frac{k}{z}(x\xi+y\eta)} d\xi d\eta \ . \tag{3.7}$$

This equation is called the Fraunhofer diffraction integral, and it is equal to a two-dimensional Fourier transform of the complex amplitude $U(\xi,\eta)$ at the aperture.
In the setup used in this thesis, a lens is used after the SLM to implement a Fourier transform just like the one in Fraunhofer approximation. Because a thin lens is used, we are able to neglect the translation of the beam inside the plane of the lens. In Figure 3.2 the geometry to perform such a Fourier transform with a thin lens is shown. Here, the lens is located at a distance d to the SLM and the imaging is performed in the distance of the focal length f of the used lens. The beam's intensity profile, that we would like to capture and investigate, will be the same as the squared absolute value of the complex amplitude in Fresnel approximation. This complex amplitude is reflected by the SLM. The coordinates u and v

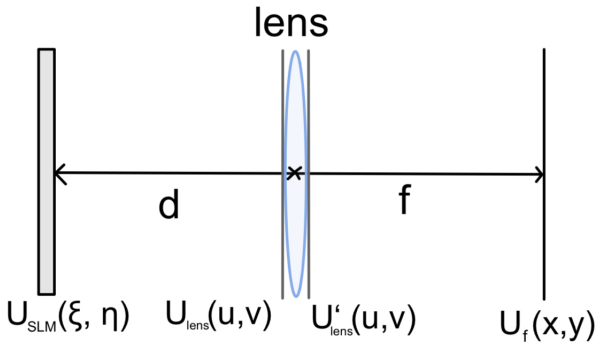

Figure 3.2: Geometry of setup where the reflected wave is represented by the scalar field U_{SLM} at the SLM, U_{lens} and U'_{lens} on the sides of the lens after a distance d and U_{f} in the focal plane f of the lens, where the light can be imaged.

represent the point where the beam enters (or exits) the lens.

The complex field amplitude in the focal plane $U_f(x,y)$ can be calculated by performing the following steps [11]:

(1) Using the Fresnel diffraction integral will lead to a connection between $U'_{\text{lens}}(u,v)$ and $U_f(x,y)$

$$U_f(x,y) = \frac{e^{ikz}}{i\lambda f} e^{\frac{ik}{2f}(x^2+y^2)} \int\int_{-\infty}^{\infty} U'_{\text{lens}} e^{\frac{ik}{2f}(u^2+v^2)} e^{-\frac{ik}{f}(xu+yv)} du dv \ . \tag{3.8}$$

(2) We can substitute the translation through the lens, which is given by $U'_{\text{lens}}(u,v) = t(u,v)U_{\text{lens}}(u,v) =$

$e^{-\frac{ik}{2f}(u^2+v^2)}U_{\text{lens}}(u,v)$ into the function calculated in step (1):

$$\begin{aligned} U_f(x,y) &= \frac{e^{ikz}}{i\lambda f} e^{\frac{ik}{2z}(x^2+y^2)} \int\int_{-\infty}^{\infty} U_{\text{lens}}(u,v) e^{-\frac{ik}{f}(xu+vy)} du dv \\ &= U_f(x,y) \frac{e^{ikz}}{i\lambda f} e^{\frac{ik}{2f}(x^2+y^2)} \mathcal{F}\{U_{\text{lens}}\}(f_x, f_y) \end{aligned} \tag{3.9}$$

where $f_x = \frac{x}{\lambda f}$ and $f_y = \frac{y}{\lambda f}$ represent the spatial frequencies. This equation presents a Fourier transform of $U_{\text{lens}}(u,v)$.

(3) Using again the Fresnel approximation will lead to a Fourier transform of $U_{\text{SLM}}(\xi,\eta)$, which can be substituted into Equation 3.9 and then be rewritten as an integral. This function is equal to the Fraunhofer diffraction integral with an additional phase factor.

$$U(x,y) = \frac{e^{\frac{ik}{2f}(1-\frac{d}{f})(x^2+y^2)}}{i\lambda f} \int\int_{-\infty}^{\infty} U_{\text{SLM}}(\xi,\eta) e^{-\frac{ik}{f}(x\xi+y\eta)} d\xi d\eta \,. \tag{3.10}$$

Finally, this yields the intensity distribution created by the SLM and the lens [11]

$$I(x,y) = |U_f(x,y)|^2 \propto \left|\mathcal{F}\{U_{\text{SLM}}(\xi,\eta)\}(f_x,f_y)\right|^2 \,. \tag{3.11}$$

One needs to emphasize that this intensity distribution is equivalent to the one in Fraunhofer approximation (Equation 3.7) and therefore the lens can be used to image the far field distribution of the reflected beam.

3.3 Operational Considerations for SLM

In this thesis a SLM manufactured by Hamamatsu, specifically the model X13267-02, is used with 792 x 600 pixels for phase modulation [27]. The pixel size is 12.5 μm. The SLM driver allows the upload of 8 bit images to the device, which means that voltage can be applied to each pixel in 256 discrete steps.

The used device itself has been tested previously in our group in the Bachelor thesis of J. A. de Haan, where the SLM was first tested, and multiple approaches were made to implement a tailored optical potential to replace or be combined with the AOD-generated traps currently in use of the RQO experiment [28].

The exact phase change obtained for a given voltage change depends on the wavelength of the incident light and on the geometry of the SLM. Therefore, the manufacturer of the SLM provides two correction options: a look-up table to correct for wavelength and a wavefront correction pattern that corrects for the shape of the SLM.

The following sections of this chapter discuss the characterization of the phase shift obtained with the SLM and the two correction options from the manufacturer.

3.3.1 Phase modulation

The manufacturer of the utilized SLM specifies that the amount of phase modulation is different depending on the wavelength λ of the used light. This implies that a phase modulation of 2π is reached at a different value of the input signal [29].

The phase shift of the light cannot easily be measured directly. Instead, the phase shift is characterized indirectly by measuring how the polarization changes. The setup used for those measurements can be seen in Figure 3.3. More details on the setup and the laser will be discussed in the next chapter. It is important to note that the SLM is not changing the polarization of the light, but that the SLM only affects horizontally polarized light. To map the phase change onto a polarization signal, incident light with linear but diagonal polarization is used. When the horizontal component of this incident light experiences a phase shift, the resulting polarization changes from linear to circular, and this change can be resolved in intensity with a polarizer [1].

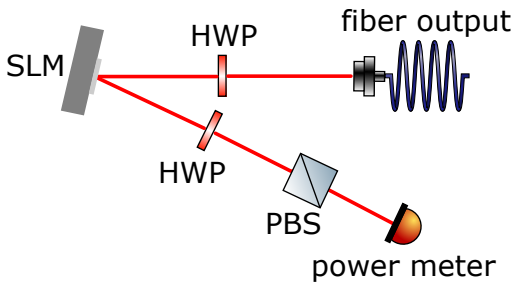

Figure 3.3: Setup for measuring the calibration curve where horizontally polarized light comes out of fiber, is reflected by SLM and detected by a power meter

The Jones matrix formalism can be utilized with fully polarized light. It describes the polarization of an electromagnetic wave in a two component vector and any polarizing optical element with a matrix [30]. The Jones vector for a plane wave propagating in z-direction can be written in terms of the components of the complex envelope in x- and y-direction

$$\vec{J} = \begin{pmatrix} A_x \\ A_y \end{pmatrix}. \tag{3.12}$$

The fiber output is known to be horizontally polarized and therefore the corresponding Jones vector is given by $|H\rangle = \begin{pmatrix} 1 \\ 0 \end{pmatrix}$.

As shown in the setup, a half wave plate (HWP) is used, to enable analysis of the phase in both x- and y- direction at the same time. A HWP is able to retard the phase of one of the axis of the electric field vector by π [30]. Therefore, it can rotate the direction of polarization by an arbitrary angle.

[1] This is also the working principle of a Pockels cell.

The Jones matrix for a HWP rotated by an angle θ is given by the expression [30]

$$J_{\mathrm{HWP}}(\theta) = \begin{pmatrix} \cos(2\theta) & \sin(2\theta) \\ \sin(2\theta) & -\cos(2\theta) \end{pmatrix}. \tag{3.13}$$

The matrix for the SLM can be expressed as

$$J_{\mathrm{SLM}}(\varphi) = \frac{1}{\sqrt{2}} \begin{pmatrix} 1 & 0 \\ 0 & \mathrm{e}^{i\varphi} \end{pmatrix} \tag{3.14}$$

where a dependency on the phase φ, with which the bit mapped image for the SLM is calculated with, can be observed. The matrix can be expressed like this because the SLM only works with horizontally polarized light to match the orientation of the LC layer [27] and introduces a phase shift for this component only. In this case, it is only effecting the A_{y} component. The Jones matrix $M(\theta, \varphi)$, which represents the polarization of the system, can be calculated as

$$M(\theta, \varphi) = J_{\mathrm{HWP},1}(\theta) \cdot J_{\mathrm{SLM}}(\varphi) \cdot J_{\mathrm{HWP},2}(\theta) \, |H\rangle \,, \tag{3.15}$$

which leads to

$$M(\theta, \varphi) = \begin{pmatrix} \cos^2(2\theta) + \sin^2(2\theta) \cdot \mathrm{e}^{i\varphi} \\ \cos(2\theta)\sin(2\theta)(1 - \mathrm{e}^{i\varphi}) \end{pmatrix} \overset{\theta=22.5^\circ}{=} \frac{1}{2} \begin{pmatrix} 1 + \mathrm{e}^{i\varphi} \\ 1 - \mathrm{e}^{i\varphi} \end{pmatrix}, \tag{3.16}$$

where it was already assumed that both HWP are set to an equal angle θ. To remove the θ dependency an angle of $\theta = 22.5^\circ$ can be chosen. Therefore, the intensity is approximated to

$$I(\theta, \varphi) \propto \left| (\cos\theta + \sin\theta) \frac{1}{\sqrt{2}} \begin{pmatrix} 1 \\ \mathrm{e}^{i\varphi} \end{pmatrix} \right|^2 = \left| \frac{\cos\theta}{\sqrt{2}} + \frac{\mathrm{e}^{i\varphi}}{\sqrt{2}} \sin\theta \right|^2 \overset{\theta=22.5^\circ}{=} \cos^2\left(\frac{\varphi}{2}\right). \tag{3.17}$$

Finally, a polarization beam splitter (PBS) is used, to only analyze the horizontal polarized part of the light and this means that the x-component of the vector vanishes [2]

$$M(\varphi) = \frac{1}{2} \begin{pmatrix} 0 \\ 1 + \mathrm{e}^{i\varphi} \end{pmatrix}. \tag{3.18}$$

The polarization of the light after each optical element can be visualized in the Poincaré sphere, which can be observed in Figure 3.4. The Poincaré sphere is often mentioned in terms of the Stokes parameters, which can also represent unpolarized or partially polarized light, the Jones vector is the same spinor just expressed in a different basis [31]. The vector points to different spots on the sphere depending on the lights polarization. Ideally, the North Pole corresponds to right hand $|R\rangle$ and the South Pole to left hand $|L\rangle$ polarized light. One needs to emphasize that the sphere is rotated here. The spots for horizontal $|H\rangle$ and vertical $|V\rangle$ polarized light lie on the equator on opposite spots. Additionally, there are also points that represent other linear polarizations, which also lie on the equator, namely diagonal $|D\rangle$ and antidiagonal $|A\rangle$ polarized light [32].

To characterize the phase shift introduced by the SLM, different uniform images of various gray levels

[2] Here the y-axis is the horizontal one.

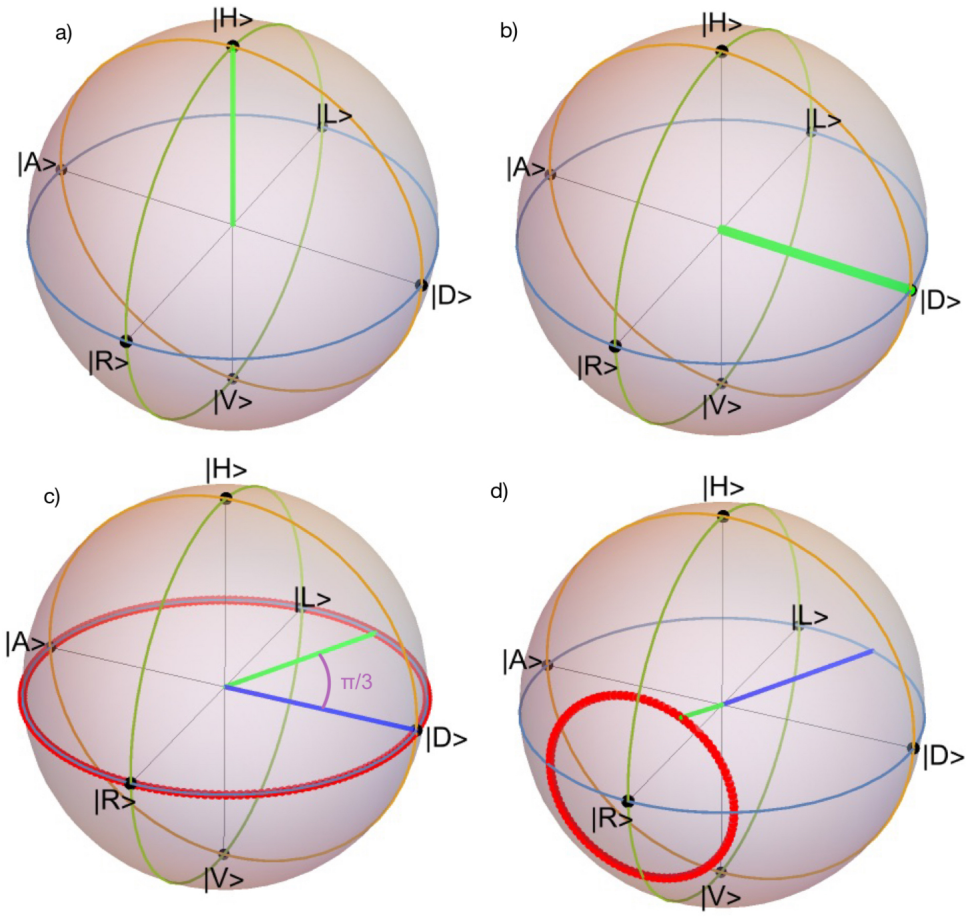

Figure 3.4: Poincaré sphere for polarization after different optical elements: a) initial polarization of horizontally polarized light, b) polarization after the first HWP set to $\theta = 22.5^{\circ}$ which is diagonal, c) polarization after SLM (for an angle of $\varphi = \frac{\pi}{3}$), here the blue line represents the polarization from before (see b), the green line denotes the new obtained polarization and the red curve shows the rotation of the green line for different values of φ, d) polarization after second HWP (φ=$\frac{\pi}{3}$, $\theta = 22.5^{\circ}$.)
The code used for the plotting of the polarization state was developed in our group using Mathematica programming language and was further modified by me.

that correspond to values of $\varphi \in [0, 2\pi]$ are displayed onto the SLM and the intensity is measured after the PBS. A phase of $\varphi = 0$ corresponds to a completely black phase mask and a phase of $\varphi = 2\pi$ to a white one, all the steps in between represent a different gray level. In Figure 3.5 the curve for the intensity modulation can be seen, which was plotted with the fitting function

$$I(\varphi) = a \cdot \cos\left(c\frac{\varphi}{2} + d\right)^2 + b. \tag{3.19}$$

where the parameters a, b, c and d are used to consider both the offset and the variation in intensity due to the phase shift and can be seen in Table A.1. The method of non-linear least squares was used to fit the function.

One also needs to emphasize that the power meter used for this experiment [3] is specified to have an accuracy of ±3% and that is where the error in every plot the device was used for a measurement occurs from.

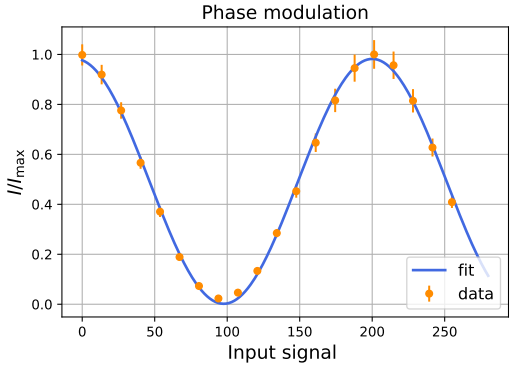

Figure 3.5: Phase modulation for normalized intensity in terms of input signal $[0, 255]$, which corresponds to a different gray levels (note that both the wavefront and the LUT setting are turned off here). Some errorbars are not visible due to the small error value.

The Michelson contrast of the intensity of the curve can be estimated by the equation [34]

$$\eta = \frac{I_{\max} - I_{\min}}{I_{\max} + I_{\min}}\,. \tag{3.20}$$

Therefore, the contrast of this curve is given by $\eta = (0.955 \pm 0.017)$. This shows that the intensity will not completely reduce to zero but to a value which is close. This might be due to other light sources in the laboratory. Another reason might be the dark current of the power meter. With an IR viewer it could be observed that a tiny part of the beam was clipped on the SLM in the initial setup and this can also contribute to this result.

To obtain the transfer characteristics, which represents a linear relation between the phase modulation and the input signal gray level, shown in Figure 3.6 one has to calculate the phase modulation for each

[3] Thorlabs PM100D [33]

input signal, which can be derived from the measured intensities

$$\varphi = 2 \arccos\left(\sqrt{\frac{I(\varphi)}{I_0}}\right) . \tag{3.21}$$

This measurement leads to a 2π phase modulation at an input signal of approximately (202 ± 2). For the used wavelength of 780 nm, the manufacturer claims that the device needs an input signal of 206 for a 2π modulation [29]. It can be seen that the measured value here is a bit smaller than the intended value (97.7 %), but still in the same order of magnitude.

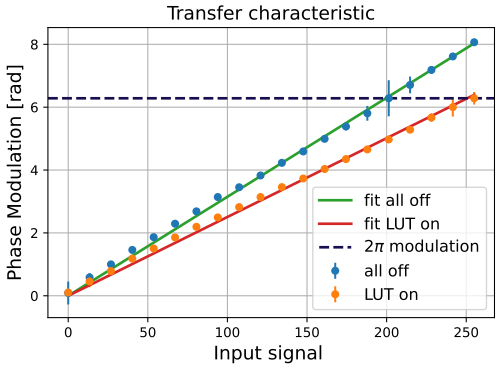

Figure 3.6: Transfer characteristics for LCOS-SLM when the phase modulation is obtained from the normalized intensities for all settings off and for LUT setting turned on. The estimated error is small and therefore cannot be seen in the plot for most values.

3.3.2 Look-up-table (LUT)

The LUT setting is a look-up-table provided in the program of the SLM, which is able to rescale the brightness value of every pixel according to the phase modulation of the used wavelength [35].

When the LUT setting is on, the 2π phase modulation is accomplished at a higher input signal compared to when it is turned off as it is shown in Figure 3.6. The phase modulation curve was also taken for the LUT setting turned on (wavefront setting is still off) for the same input signals. This plot can be seen in Figure 3.7. The 2π phase modulation is reached after an input signal of approximately (246 ± 5).

Therefore, it is assumed that the LUT setting rescales the applied voltage such that it is limited to some lower value at 255 than what is applied without LUT. With Equation 3.20 the contrast of this curve was calculated to be $\eta = (0.959 \pm 0.017)$, which is slightly bigger but almost equivalent to the value of LUT being turned off.

3.3.3 Wavefront setting (WF)

The wavefront of the reflected light on the SLM exhibits a fixed distortion, which is produced by the silicon back plane of the CMOS chip [27]. This principle is portrayed in Figure 3.8. To compensate for

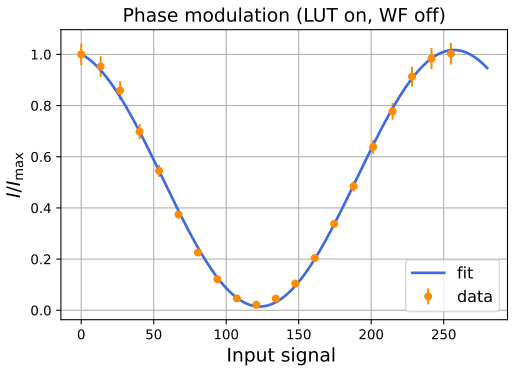

Figure 3.7: Phase modulation for LUT setting turned on but WF setting still off. The normalized intensity is plotted in terms of input signal and the fit parameters can be seen in Table A.1. Some errorbars are not visible due to the small error value.

this distortion, flatness correction data is provided for different wavelengths in the program, which is used when the wavefront setting is turned on. The image correction data is superimposed with the phase image on the SLM when the option is turned on [35].

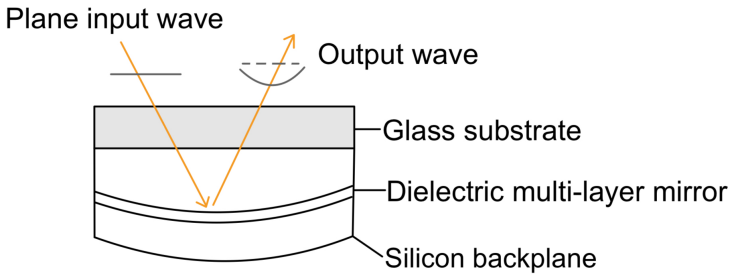

Figure 3.8: Wavefront distortion caused by the silicon back plane of the CMOS chip (based on image in [27])

The phase modulation was also measured for when the wavefront setting is turned on, which is shown in Figure 3.9. Just like the other curve with LUT turned on, the 2π modulation is reached at a higher input signal of (253 ± 4). It can be seen that the contrast of the intensity decreased compared to when the WF setting is turned off to a value of $\eta = (0.668 \pm 0.012)$. Additionally, the first few data points taken here do not seem to represent the $\cos^2\left(\frac{\varphi}{2}\right)$ curve. It is still not totally clear why this is the case.

In Figure 3.10 we can recognize the phase modulation curve for both of those two settings turned on. Just like the curves portrayed before for one of both settings turned on, the 2π modulation is accomplished after a higher input signal of (254 ± 2). Here the contrast is also smaller than for both settings turned off and results in a value of $\eta = (0.728 \pm 0.098)$.

It also needs to be emphasized that the WF setting was not used for further measurements because it decreased the contrast and led to unexpected curve behavior. Later, it could be seen that the beam

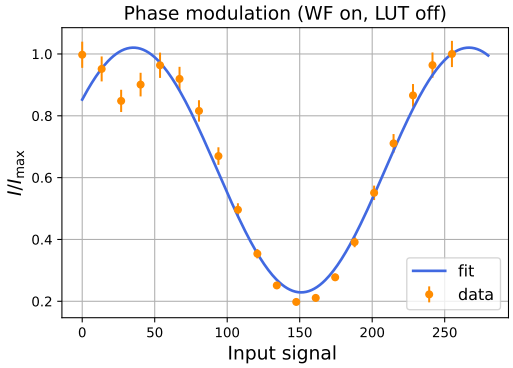

Figure 3.9: Phase modulation for LUT turned off but WF setting on. The normalized intensity is plotted in terms of input signal and the fit parameters can be seen in Table A.1. Some errorbars are not visible due to the small error value.

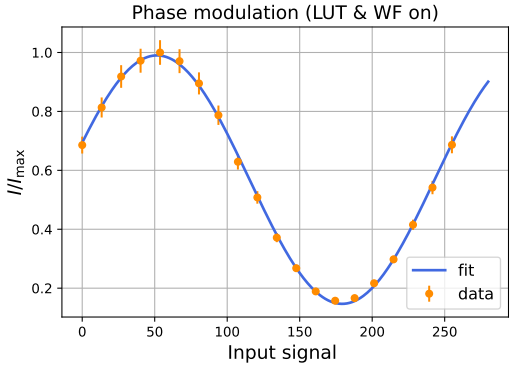

Figure 3.10: Phase modulation for both the LUT and WF setting on. Some errorbars are not visible due to the small error value. The fit parameters can be distinguished from Table A.1.

seemed to be elongated in one direction when turning this setting on.

3.3.4 Diffraction efficiency

According to the manufacturer, the used SLM is characterized by a high diffraction efficiency [27]. Therefore, the diffraction efficiency can be calculated by the following equation

$$\xi = \frac{I_{1\text{st}}}{I_0}\,, \tag{3.22}$$

where $I_{1\text{st}}$ represents the intensity in the first diffraction order and I_0 denotes the intensity associated with the zeroth order in the absence of any displayed pattern, where the SLM just works as a mirror. The measured data points can be observed in Figure 3.11. Here, the diffraction efficiency is measured in terms of the spacial frequency, which is given in the unit line pairs per mm (lp/mm). For example, a two level grating consists of one dark and one bright line and is equal to 40 line pairs

per millimeter in this case because of the pixel size of the used SLM. We can notice that a higher spatial frequency will result in a lower diffraction efficiency. In return, this implies that the diffraction efficiency is the best for a position that is near the zeroth order spot. Therefore, a grating with multiple gray levels will result in a higher diffraction efficiency, because the first order is closer to the zeroth one.

A value of five lines per millimeter is equal to a twelve level grating, but unfortunately it was not possible to measure the intensity I_{1st}, due to experimental limitations. It can be seen that for a blazed grating that contains more steps of gray levels, the diffraction efficiency shows a bigger deviation to the values provided in the manual. In principle, the measured diffraction efficiency is a bit smaller than it should be [29]. This can also be a result of an angle of incidence, that was chosen to be too large in the initial setup.

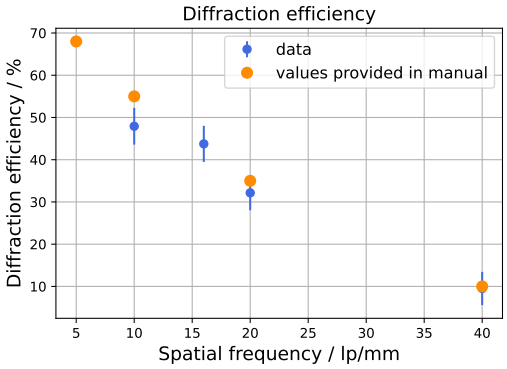

Figure 3.11: Measured diffraction efficiency in terms of the spacial frequency compared to values provided in manual [27]

CHAPTER 4

Detection of different OAM beams

Based on the ideas and work presented so far, the next goal is to modulate the phase of an initial Gaussian beam into a LG beam by applying a phase mask onto the SLM. In this chapter we will first discuss how a phase mask can be generated, and it will also be shown what they look like. Furthermore, it is explained how a blazed grating can be utilized to image certain modes in the first order of diffraction. The setup of the experiment is visualized, and each element is explained. Additionally, the measured threshold curve for the used laser is shown and in particular the two telescopes used in this setup are characterized, where one of them performs a Fourier transform of the wavefront just as predicted in section 3.2. Afterwards, some of the detected LG and HG beams are shown. Because the results here can still be improved, a method to do so is presented, which leads to another set of experimental results. Finally, the experimentally taken data is compared to the theoretical expected solutions, that were presented in chapter 2.

4.1 Techniques in Phase Pattern Generation

To transform a Gaussian beam into various LG or HG modes we will make use of different phase masks, which can be displayed onto the SLM to modulate the phase of the laser beam.

4.1.1 Design and implementation of complex phase patterns

Earlier, the intensity distributions of HG and LG modes were used to implement the simulations of the different modes. Now, the derived function of the complex amplitude for a wave propagating in z-direction is considered to generate the phase masks. For this use we will need to remember that the complex amplitude of a plane wave is given by $U(\vec{r}) = A(\vec{r}) \exp(-ikz)$.

We can use the properties $A(\vec{r}) = |U(\vec{r})|$ which is the amplitude of the wavefront and $\phi(\vec{r}) = \mathrm{Arg}(U(\vec{r}))$ which represents the phase of an optical field at the plane $z = 0$. The following phase profile Ψ can be used to implement the phase masks

$$\Psi(x, y) = \mathrm{Mod}\left[\phi(x, y), 2\pi\right] \ . \tag{4.1}$$

This leads to the phase masks shown in Figure 4.1 for LG modes and Figure A.2 for HG modes.

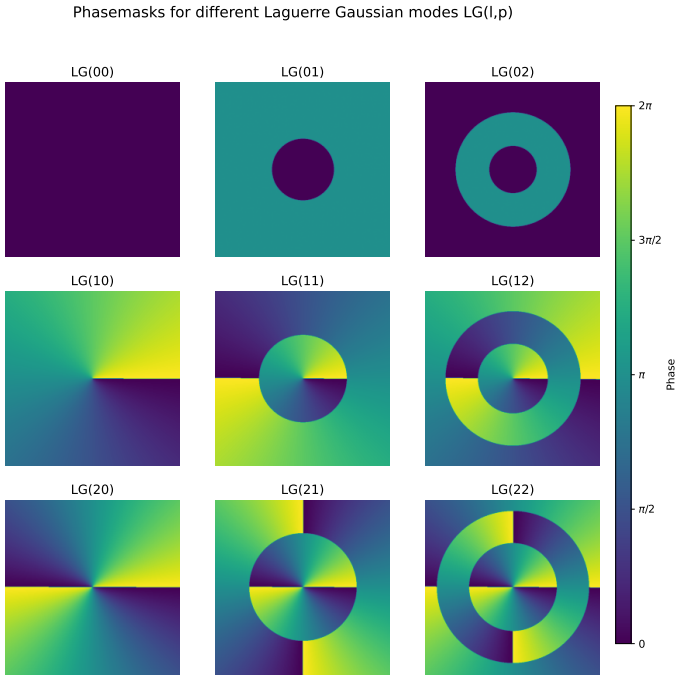

Figure 4.1: Phase masks for different Laguerre-Gaussian modes

4.1.2 Utilizing gratings for precision phase modulation

To create non-Gaussian beams with a SLM, it will be necessary to separate the generated beam from a zero order beam. Here, the same approach is used as in the paper by Alicia V. Carpentier et al. [36], where the SLM is used as a grating that can shift the beam in space. This results in the phase profile of

$$\Psi(x, y) = \text{Mod}\left[\phi(x, y) + \frac{2\pi x}{\Lambda}, 2\pi\right] , \tag{4.2}$$

where Λ characterizes the period of the blazed grating. The first term in the equation can be represented by a helical wave (for LG modes), whose phase pattern has been implemented in the last subsection. The second term denotes a blazed grating. The benefit of such a grating is that the initial Gaussian beam is diffracted into a series of diffraction orders, which position is dependent on the parameter Λ. When adding both terms together, a fork grating is created (for LG beams), which can be seen in the additional material. The principle of this mathematical method is shown in Figure 4.2.

If the phase masks for the LG modes are applied, one can observe a diffraction grating for which the zeroth order represents an ordinary Gaussian beam. In higher orders of the diffraction pattern optical vortices with different topological charges $\pm ml, l \neq 0$ can be detected, where $\pm m$ characterizes the diffraction order ($m = \pm 1, \pm 2, ...$). The sign of the diffraction order indicates a different helicity of the wavefront depending on whether the beam is diffracted to the right- or left-hand side of the undiffracted

beam [37]. All the images are taken in the first order, because in the second one we will observe a beam of higher order.

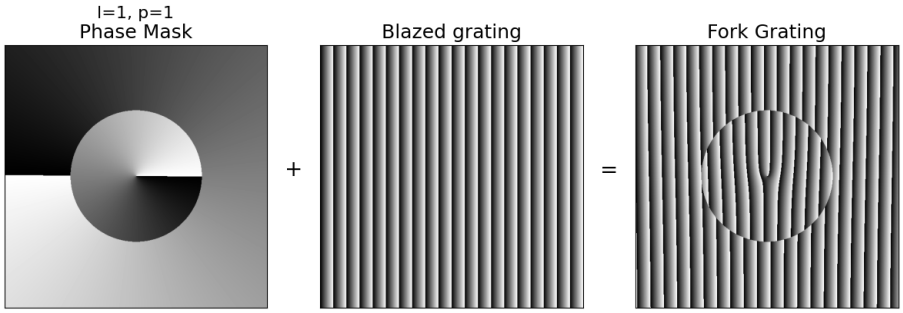

Figure 4.2: Principle to obtain a fork grating: adding a phase mask and blazed grating

4.2 Experimental setup

The light source for the experiment is a laser, which is fiber coupled to clean the beam shape, and is then reflected off the SLM before it is focused onto a camera. A sketch of the setup is shown in Figure 4.3 and in the following, the individual parts are discussed.

The laser is a 780nm extended cavity diode laser [38]. An optical isolator is placed at the output of the laser, which is able to protect the laser from back reflections that could possibly damage it [39]. The isolator is making use of the Faraday effect to extinguish reflections.

After the optical isolator, the intensity of the laser is adjusted with neutral density (ND) filters. By placing the filters before the light is fiber coupled and not for instance right in front of the camera possible interference effects are avoided.

Because the polarization output of the laser is linear vertical and the light that is needed to match the LC layer of the SLM is horizontally polarized, a HWP is used to align the polarization and couple the light into a polarization maintaining single mode fiber. In order to make sure that the light is polarized horizontally before hitting the SLM a single PBS is used to check, which only transmits the horizontally polarized field component. I measured that almost 98% of the light was transmitted. Afterwards, a single mode fiber is utilized to create a Gaussian beam shape. An out coupling lens with a focal length of $f = 11$mm is used. The fiber output is guided through a telescope, which acts as a beam expander, so that the beam size matches the size of the effective area of the SLM. The effective area describes the area of the SLM where the hologram is portrayed. Different holograms can be uploaded and spatially change the phase of the laser beam. One also needs to emphasize that a small angle of incidence is needed for the SLM. It is recommended to use an angle of incidence of $\theta \leq 5^\circ$ [27], where θ denotes the angle between the normal of the SLM and the incident laser beam. If an angle greater than zero is chosen, the pixel size in one direction d_x will increase to a value of $d'_x = \frac{d_x}{\cos(\theta)}$ [28] and the pixels cannot be

assumed to be quadratic anymore. Therefore, the image size will increase in that direction. To reduce this effect, the smallest possible angle is chosen.

To be able to image the beam after modulating it with the SLM, we use a second telescope, which reduces the beam size. The combination of the lenses gives an effective lens that Fourier transforms the complex wavefront that has been mathematically derived in section 3.2.
Finally, the beam can be imaged on a camera [1] placed in the focal plane of the telescope.

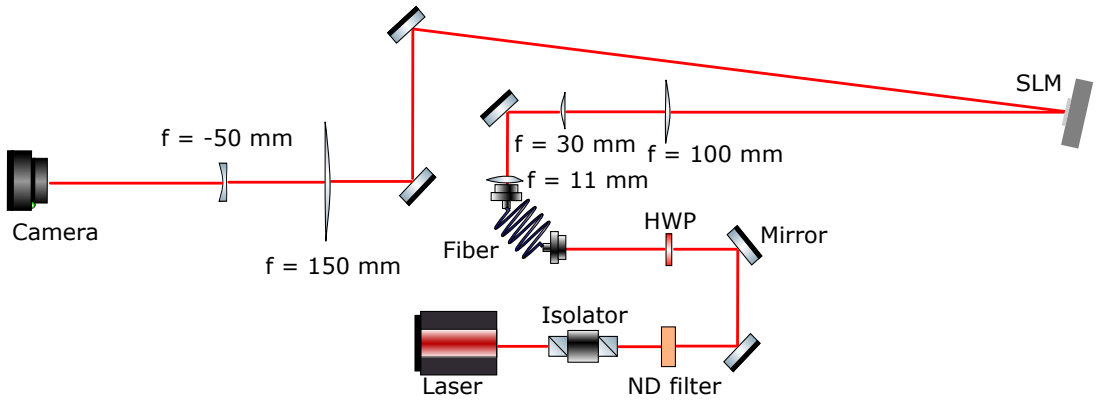

Figure 4.3: Setup used to capture different modes on camera (discussed in main text)

4.2.1 Laser threshold

The used laser in this thesis operates at a wavelength of 780 nm. The manufacturer specifies its laser to have a threshold current of 30 mA [38]. Before constructing the experimental setup, it was checked whether the lasing threshold is still as specified in the data sheet. A threshold measurement was performed, which can be seen in Figure 4.4. One can observe the measured power in terms of the current I, which leads to a measured threshold value of (31.87 ± 0.28) mA. The threshold value is obtained from the interception with the x-axis of the fit. The result of this measurement is slightly bigger than the value provided in the manual. Previous usage of this laser in our group let to a threshold value of 33.2 mA.

4.2.2 Magnification of the telescopes

As already mentioned, the first telescope after the fiber output is used to match the size of the beam to the effective area of the SLM. For this to work, one first has to measure the beam's waist after the fiber coupler at various distances to make sure that the beam is collimated. This is done with a camera[2]. The beam's waist is extracted by doing an one dimensional Gaussian fit in both the vertical and the horizontal direction. The mean value for the waist was measured to be (1.161 ± 0.015)mm in the vertical direction and (1.074 ± 0.004)mm in the horizontal direction. The fit for the horizontal and vertical waist sizes for

[1] Here an Unibrain Fire-i 530b camera was used [40].
[2] For this measurement, the camera Arducam MT9J003 was used [41]. Due to severe interference effects on the taken images all the other images were taken with the Unibrain camera.

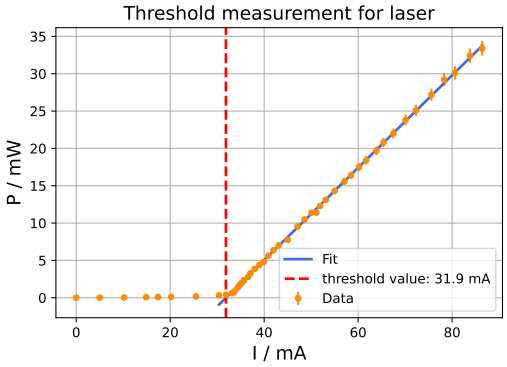

Figure 4.4: Threshold measurement for laser used in this thesis where the power of the laser is measured in terms of the current. Errorbars are not visible due to the small error value. This measurement was also performed a power meter [33].

different positions relative to the out coupling lens is shown in Figure A.4. Because the obtained waist sizes are not equal, we calculate the eccentricity [42]

$$e = \sqrt{1 - \frac{b^2}{a^2}}\,, \tag{4.3}$$

where a denotes the vertical axis of the beam and b the horizontal one. For a perfect circle the eccentricity should be equal to zero. We calculate a value of $e = (0.378 \pm 0.031)$ and see that the beam is slightly elongated. Another, more convenient way while working on the setup is to use a so-called shear plate interferometer to aim for a collimated beam. This approach was done afterwards to optimize the results.

The mode field diameter of the used fiber is $(5.3 \pm 1.0)\mu$m [43]. When the geometry of the setup is taken into account, one can see that the waist after the fiber coupler W_1 can be calculated with $W_1 = \tan(\theta) \cdot f + W_0$, where $f = 11$mm denotes the focal length of the out coupling lens and W_0 is equal to the mode field diameter. From Equation 2.13 we obtain an angle of divergence of $\theta = (0.094 \pm 0.018)$. Therefore, we obtain a value of $W_1 = (1.039 \pm 0.019)$mm. One can see that this value matches the experimental findings with some deviation in vertial direction.

For the magnification a refracting telescope is used and therefore the waist of the beam after the telescope can be calculated by $W_2 = \frac{f_2}{f_1} W_1$, where f_1 represents the focal length of the objective (first lens) and f_2 of the second lens. To match the size of the effective area of the SLM, which is given by 9.9 times 7.5 mm, we choose a ratio of $\frac{f_2}{f_1} = \frac{100\text{mm}}{30\text{mm}} = 3.33$. Accordingly, an expected waist size of approximately 3.5 mm can be calculated after the telescope with a Gaussian beam calculator [44].

The expected image size after the SLM can be calculated with the following equation [45]

$$D = \frac{\lambda f}{L} N\,, \tag{4.4}$$

where f represents the focal length of the Fourier lens used behind the SLM, L stands for the length of

the effective area of the SLM in one direction and N describes the number of pixels in this direction. One can notice that the image size is directly proportional to the focal length of the used lens and therefore the image size can be increased by using a lens with a bigger focal length.

To fulfill space limitations, a telescope is chosen instead of a single lens to perform the Fourier transform of the wavefront. To save even more space, a concave and a convex lens are used instead of two convex ones. This second telescope is used as a beam reducer so that the camera can still image the obtained pattern. Here, the lenses are positioned at a distance not equal to the sum of their focal lengths (considering that f_2 is negative, thus the distance should be 10 cm), as we don't require a collimated beam. Instead, our aim is to capture the image in the focal plane of the telescope to achieve a Fourier transform. In this setup, the lenses are positioned at a distance of roughly 11 cm. According to a Gaussian beam calculator, the focal plane is approximately 29 cm away from the first lens [44]. Hence, the camera is placed at this location.

Ideally, a beam propagation axis should coincide with the center of a phase mask. To compensate for a possible offset, the SLM mask center was shifted. The goal was to achieve a symmetrical intensity distribution for the higher order modes of light. The center of the effective area of the SLM is located at 396 pixels in x-direction and 300 pixels in y-direction. But here a center at 450 pixels in x-direction and 250 pixels in y-direction is chosen instead. Later, it was attempted to move the SLM to verify that the laser beam is positioned at the center of its effective area. Because of the rectangular symmetry of the HG modes, it is easier to find the optimal setting for the intensity to be equally distributed. This is also shown in Figure 4.5. In the left image we observe that the right part of the mode is brighter. Therefore, the phase mask is shifted on the horizontal axis and a more equally bright mode results.

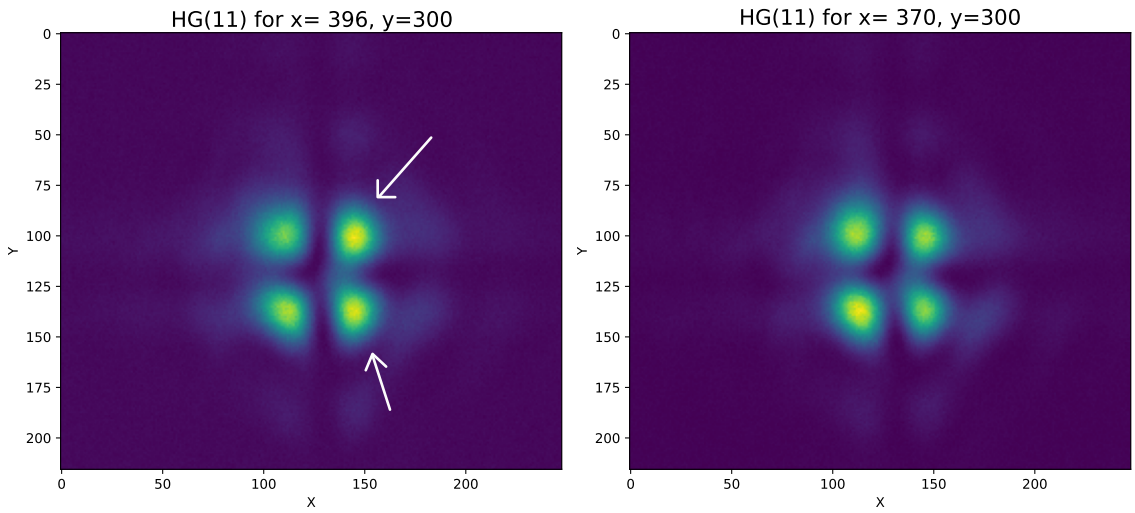

Figure 4.5: Intensity distribution of HG(11) for different positions on the x-axis. For the initial position (shown on the left) one part of the mode is significantly brighter. When the mask is shifted horizontally (right image) the mode has a more equally distributed brightness.

4.3 Experimentally taken images of different OAM beams

In Figure 4.6 we can see images of different LG modes using a hologram, which is created by using a phase mask and adding a grating on top, as described in subsection 4.1.2 and is then displayed onto the SLM. It has to be mentioned that for all the plots of the captured images, the x- and y-axis are in the unit of pixels. The different modes can clearly be identified, but the beam shape is distorted and deviates from the expected intensity distribution. To emphasize the difference between the taken data and the theory, we compare the mode LG(12) for example, shown in Figure 4.7. It can clearly be seen that the intensity is not equally distributed along the whole circumference. The left and right part of the circle carry a higher intensity than the part above and below the center.

For $l = 2$ one can notice that the inner circle seems to be divided into two smaller circles, or to be more precise ellipses. We also observe that the outer part of the modes does not look sharp and some blurring occurs. The beam's shape appears to lack circular symmetry, exhibiting elongation instead, which is particularly noticeable for $p = 1$.

At first glance, it is evident that the size of those modes is extremely small and because of the low resolution a waist fit is not very meaningful.

It is also crucial to mention that the best images could be obtained when both the WF and the LUT settings were turned off. The WF setting occasionally results in a form that deviates significantly from the intended shape.

4.3.1 Detection of different HG modes

Even though HG beams do not carry OAM and therefore are not that much of interest for the outcome of this thesis, it is still useful to capture them on camera. Because of their rectangular symmetry it is more convenient to find a position for the hologram where the intensity seems to be equally distributed. The captured images can be seen in Figure 4.8.

As for the LG beams, the HG beams are also distorted compared to what they are expected to look. Especially noticeable is the blurring of the outer part of their structure, particularly for higher modes. In Figure 4.9 this phenomenon can be seen best for the HG(22) mode. It is even extremely hard to identify the outer part of the mode. For smaller modes like HG(01) or HG(11) the image looks more appropriate because the vanishing of some parts of the mode does not occur in such a significant way. Additionally, it can be seen that for higher modes the part in the center seems to be the brightest even though the theory states the opposite. It also becomes clear that the modes have a small size just like the LG modes and that is why fitting the waist is not convenient here.

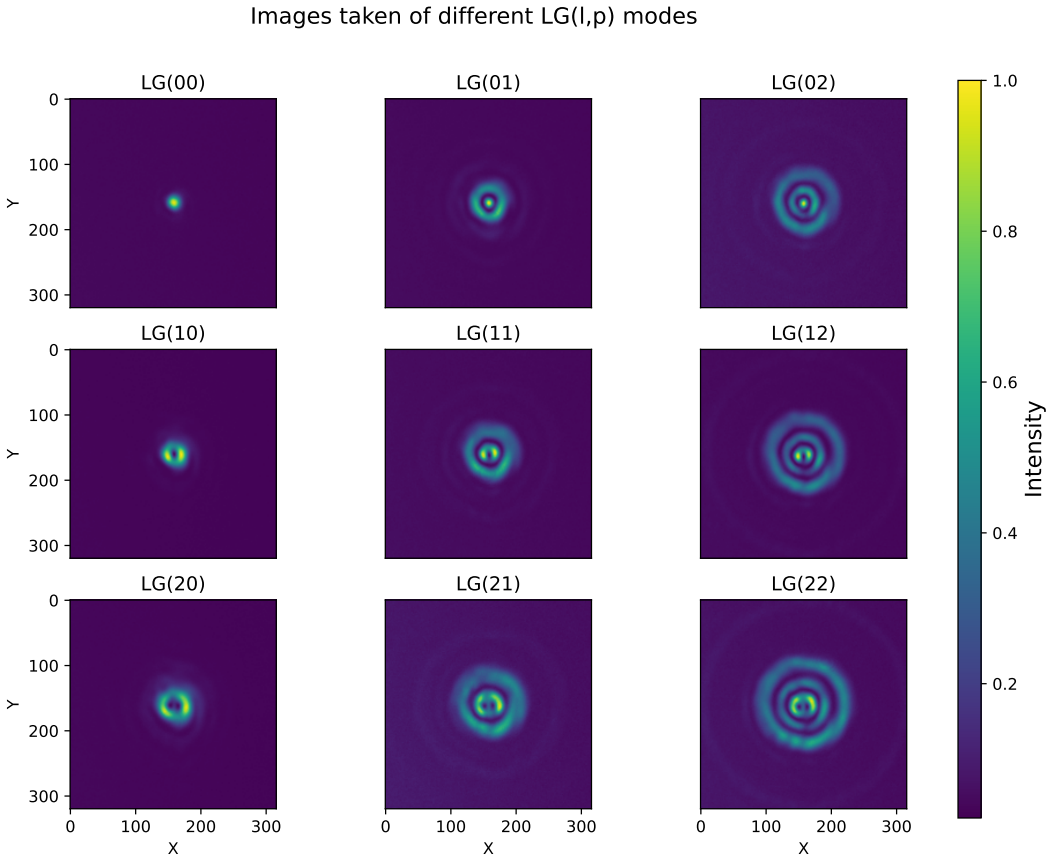

Figure 4.6: Experimentally taken images of different LG modes

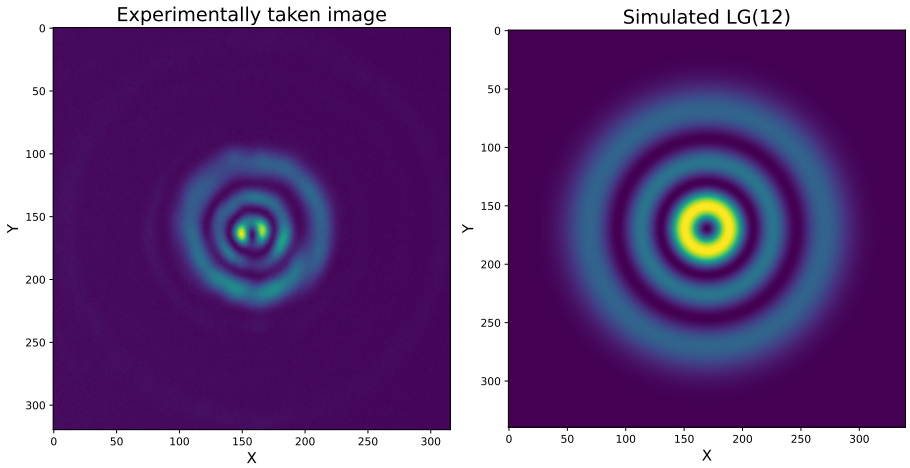

Figure 4.7: Experimentally taken image of LG(12) compared to the one obtained from theory

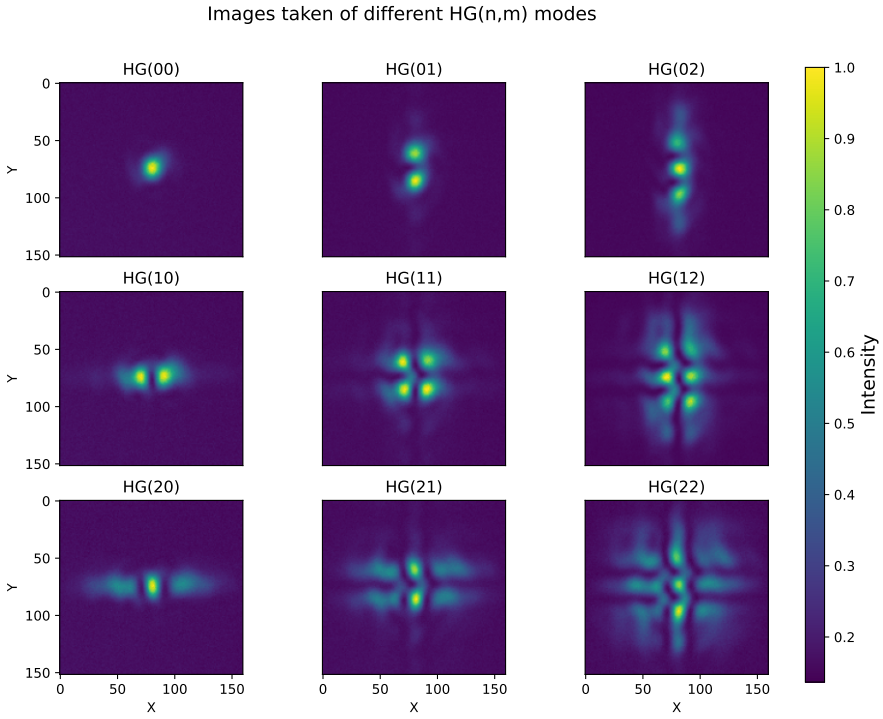

Figure 4.8: Experimentally taken images of different HG modes

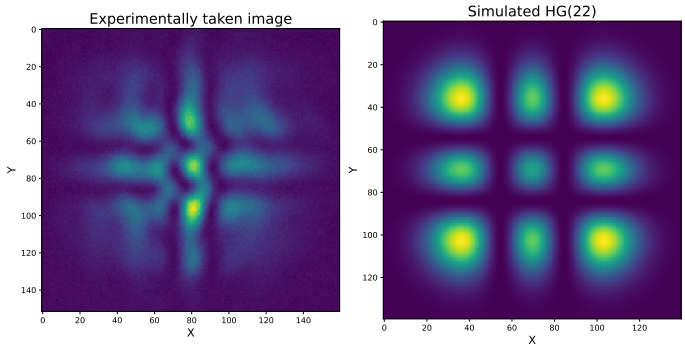

Figure 4.9: Experimentally taken image of HG(22) compared to the one obtained from theory

4.4 Optimization Methods

So far, phase-only holograms were discussed. However, there is also the method to modulate the amplitude and phase both at the same time on a phase only SLM, which could potentially result in a more accurate beam, which is imaged. This method has been presented in a paper by Bolduc et al. [46].

The basic idea is to use a grating pattern where the diffraction efficiency can be modulated by an amplitude function. The aim of using this additional function is to only diffract the desired part of the beam into the first diffraction order. The concept is shown in Figure 4.10, where the mode LG(10) is considered as an example. A slice of the phase mask along the x-axis with $y = 0$ is shown. In the first plot we observe a grating, which diffracts the light into different orders, as denoted by the arrows. The second plot shows a mirror, where the light is reflected in the same direction. The third plot represents the optimization method, that will be presented here, which can be described as an intermediate principle of the other two. We try to only get diffraction from the desired part of the beam due to the amplitude mask, which is used to modulate something similar to a mirror here.

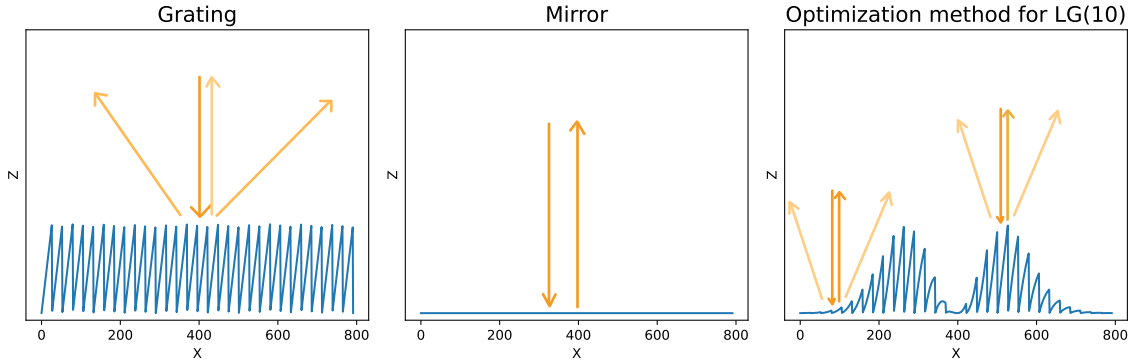

Figure 4.10: Principle of the used optimization method where we only look at a slice of the phase mask along the x-axis. In the plot for the grating the light is diffracted into different orders, for the mirror the light is reflected in the same direction and the optimization method makes use of both, thus only diffracting the desired part in the first order.

Earlier, the phase profile was implied in Equation 4.2. In the first diffraction order the output field distribution is given by

$$U_{\text{out},1} = \mathcal{F}\{\exp(i\phi(x,y))\}\,, \tag{4.5}$$

where $\mathcal{F}$ represents a Fourier transform, just as predicted in section 3.2. But now the amplitude is also considered, and therefore the equation can be modified in the following way

$$\Psi(x,y) = \mathcal{M}(x,y) \cdot \text{Mod}\left[\mathcal{K}(x,y) + \frac{2\pi x}{\Lambda}, 2\pi\right]\,, \tag{4.6}$$

where the function $\mathcal{M}(x,y)$ denotes the normalized positive amplitude function ($0 \leq \mathcal{M} \leq 1$) and $\mathcal{K}(x,y)$ represents the analytical function of the amplitude and phase profiles of the desired field. Just after the beam is reflected by the SLM, which now contains the new phase mask, the phase profile is

given by

$$U'_{\text{out}} = \exp\left(\mathcal{M}(x,y)\cdot \text{Mod}\left[\mathcal{K}(x,y)+\frac{2\pi x}{\Lambda}, 2\pi\right]\right) . \tag{4.7}$$

To obtain the phase profile in the first order of diffraction a Taylor-Fourier expansion is performed, which leads to the following term

$$U'_{\text{out},1} = -\text{sinc}(\pi\mathcal{M}-\pi)\text{e}^{i(\mathcal{K}+\pi\mathcal{M})} . \tag{4.8}$$

This expression will give us the functions needed to modulate the amplitude on a phase-only SLM

$$\begin{aligned}\mathcal{M} &= 1+\frac{1}{\pi}\text{sinc}^{-1}(A)\\ \mathcal{K} &= \phi-\pi\mathcal{M}\end{aligned} \tag{4.9}$$

where A represents the amplitude of the wavefront.
The unnormalized sinc function is defined by $\text{sinc}(x) = \frac{\sin(x)}{x}$ where $x \neq 0$. However, it can be quite difficult for an ordinary computer to calculate the inverse sinc function for every pixel. Therefore, one can use the simplification of $\mathcal{M} = A$ and $\mathcal{K} = \phi$, already mentioned by Davis et al. [47], which can also already contribute to an improvement of the beam shape. It can be shown, that the difference between the obtained amplitude and the desired one is no further apart than 16.1% [46]. The difference in phase is quite bigger and that is why it needs further modification to $\mathcal{K} = \phi - \pi A$. If those approximations are used, it leads to an output close to the desired one.

The phase masks for LG and HG modes, that were implemented with the just described method, can be observed in Figure 4.11 and Figure A.5. One needs to emphasize that those masks were not implemented with the sinc function yet, but instead with the mentioned simplification.

4.4.1 Improvement of results with optimization method

Using the already presented method of optimization with the goal of only diffracting the desired part of the beam into the first order of diffraction, we are able to see a huge improvement in the beam shape and intensity distribution of different modes.

In Figure 4.12 the different LG modes, which were captured with the optimization strategy, are shown. The first thing to notice is that the beam is significantly larger, which is due to the added amplitude mask. We also observed that the intensity is more equally distributed. However, it seems like the upper and lower part of the circles carry a slightly higher intensity than the parts on the sides of the center. The images taken here are way more similar to the simulated ones than the images without the applied optimization method. The waist sizes were also calculated for this case and are presented in Figure 4.13. It becomes clear that for the modes LG(00), LG(02) and LG(10) the waist size is larger than for the other modes. Unfortunately, it is still unclear why this is the case. For the rest of the modes, the measured waists lie in a range close to each other.

For a better comparison, the mode LG(12) is shown next to the one we expect from theory in Figure 4.14. The imaged modes will be further compared to the theoretically predicted ones in the next section.

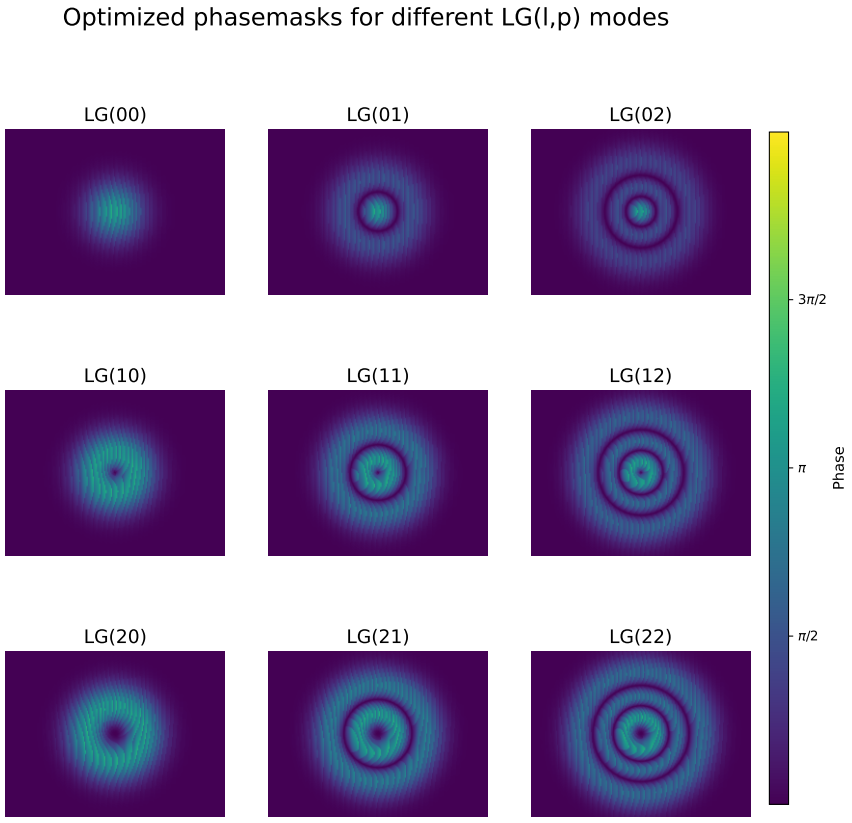

Figure 4.11: Optimized phase masks for different LG modes

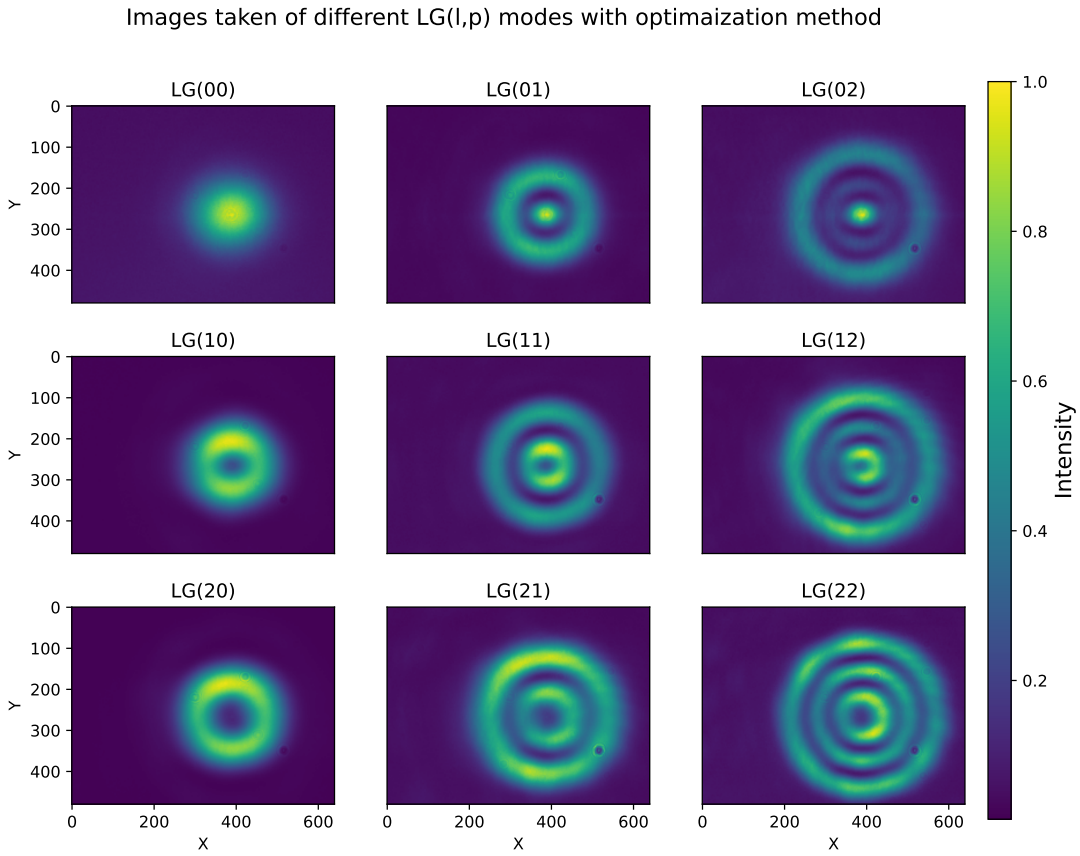

Figure 4.12: Experimentally taken images of different LG modes with optimization method

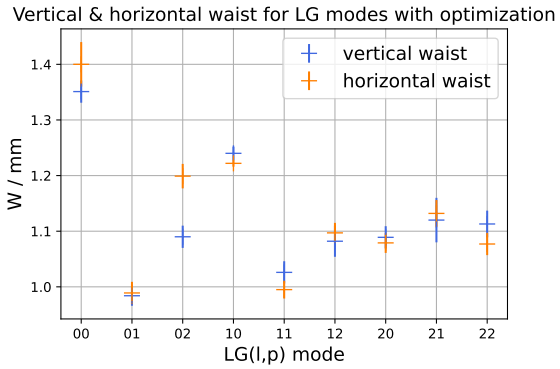

Figure 4.13: Measured waists for different LG(l,p) modes with optimization method

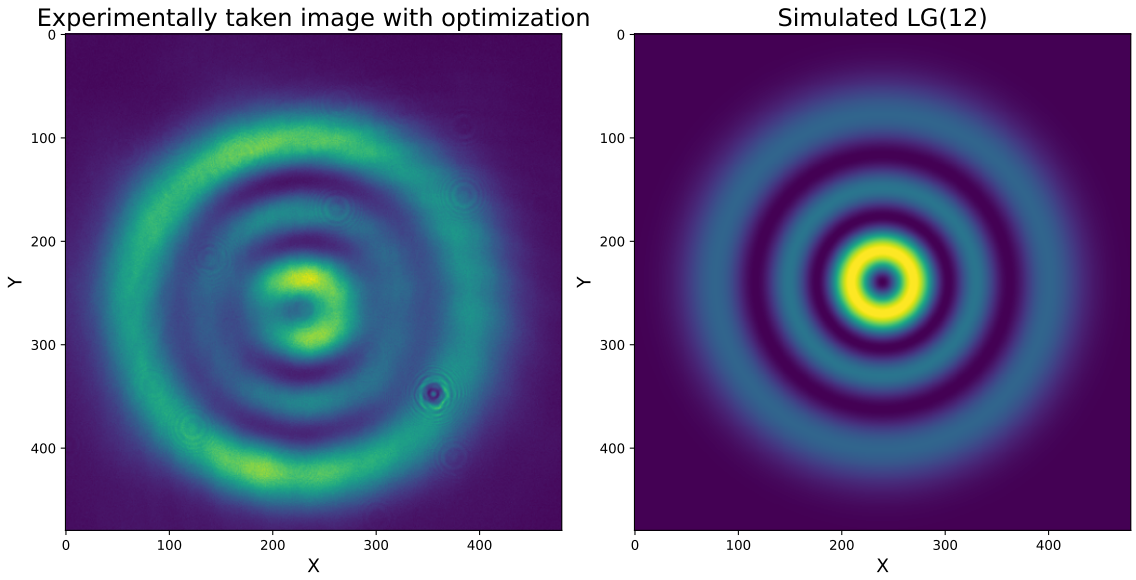

Figure 4.14: Experimentally taken image of LG(12) with applied optimization method compared to the one obtained from theory

The optimization method was also applied for the HG modes, which can be seen in Figure 4.15. Here we can also clearly notice a huge improvement compared to the images taken without the optimization method. The blurring of the outer part is not that much of an issue anymore, and we can also observe that the intensity distribution is much closer to the simulated one, where the center part was not the brightest for a lot of modes. The different waist sizes were calculated and plotted as shown in Figure 4.16. It becomes clear that the waist size increased and most of the values lie in a close range. However, we can also see that the obtained waist size for the HG beams is slightly bigger than the one for the LG beams, and this is due to rearranging the setup again in between taking the images. The distance between the two lenses of the second telescope was probably not equivalent.

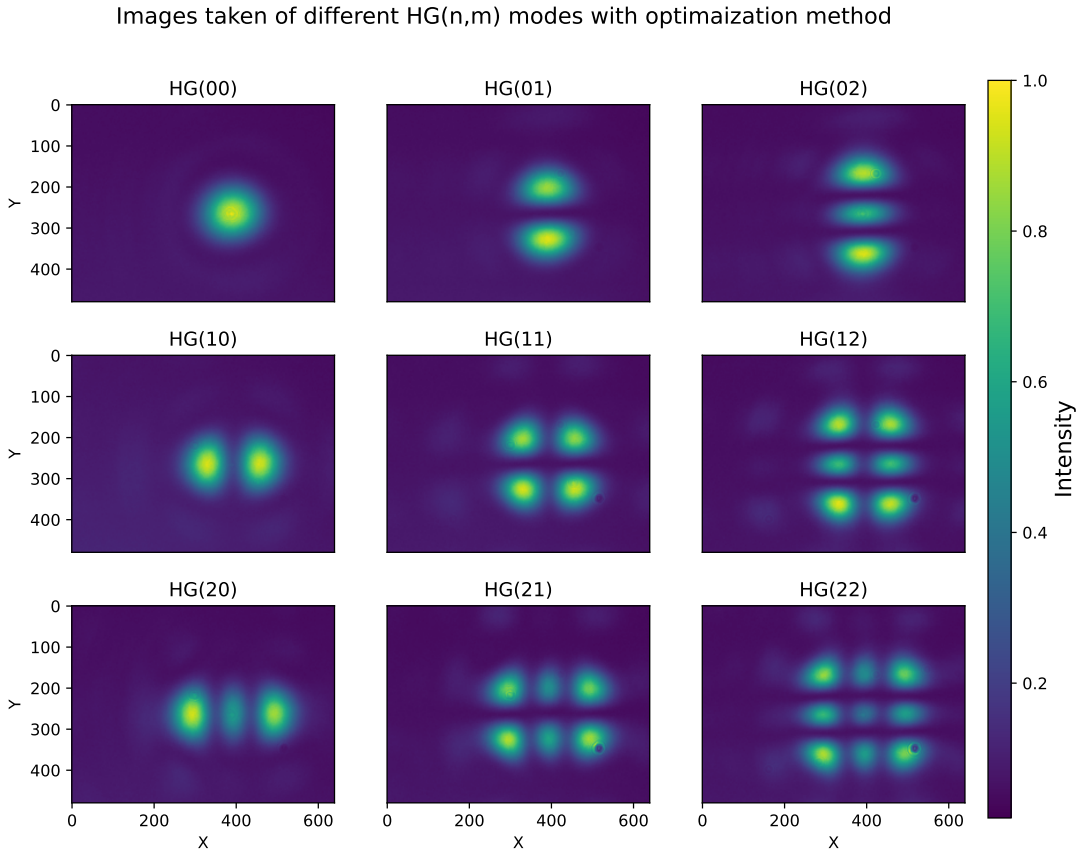

Figure 4.15: Experimentally taken images of different HG modes with optimization method

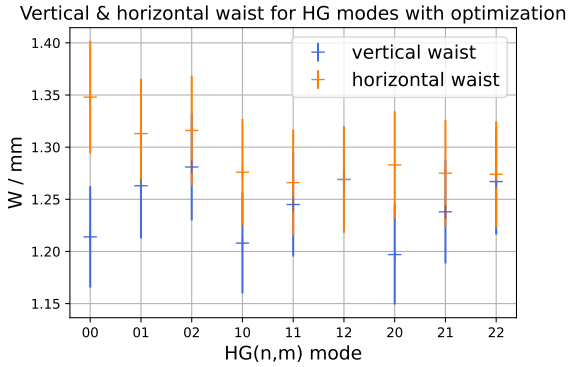

Figure 4.16: Measured waists for different HG(n,m) modes with optimization method

4.5 Comparison with theory

To compare the captured images with the ones obtained from theory, the experimentally taken data is subtracted from the simulated images. The simulation of the derived theory is shown in Figure 2.3. We make sure that both of the images are normalized. In Figure 4.17 we can observe this calculated difference for various LG modes.

It needs to be emphasized that both negative and positive values are a possible outcome. For a negative result the experimental data has bigger values and for positive results the experimental data is smaller than the theoretical one. It is important to mention that an intensity equal to zero corresponds to a different color now than in the plots earlier.

The patterns we see after subtracting suggest that there is a difference in the brightness of the rings form the modes. It was tried to shift the simulated image on the x- and y-axis manually to obtain an image, where the simulated mode overlaps with the experimentally taken data. It was also attempted to scale the images to the identical size.

Ideally, the difference of the experimental data and the theoretical one should result in zero, because this implies that both images are equal. For the LG(10) mode the least intensity can be identified after the subtraction. A structure in the middle is observed, which could be a result of some interference effects of the glass, that is placed on top of the Unibrain camera. The same observation applies to the remaining modes as well. Some artifacts can occur due to exposure of too high power on the camera. The blurring observed in the experimentally taken data also causes influences in the difference.

In the simulated images, the inner ring consistently appears noticeably brighter than the outer ones. This trend is also present in the imaged data, although the difference in brightness is not as predicted. While the inner ring remains the brightest region in most images, the outer ring appears brighter than expected. This could possibly be caused by working close to saturation of the camera. In the next iteration the laser power on the camera could be reduced.

For the modes where $p = 0$, we are confronted with the same issues. The simulation states that the

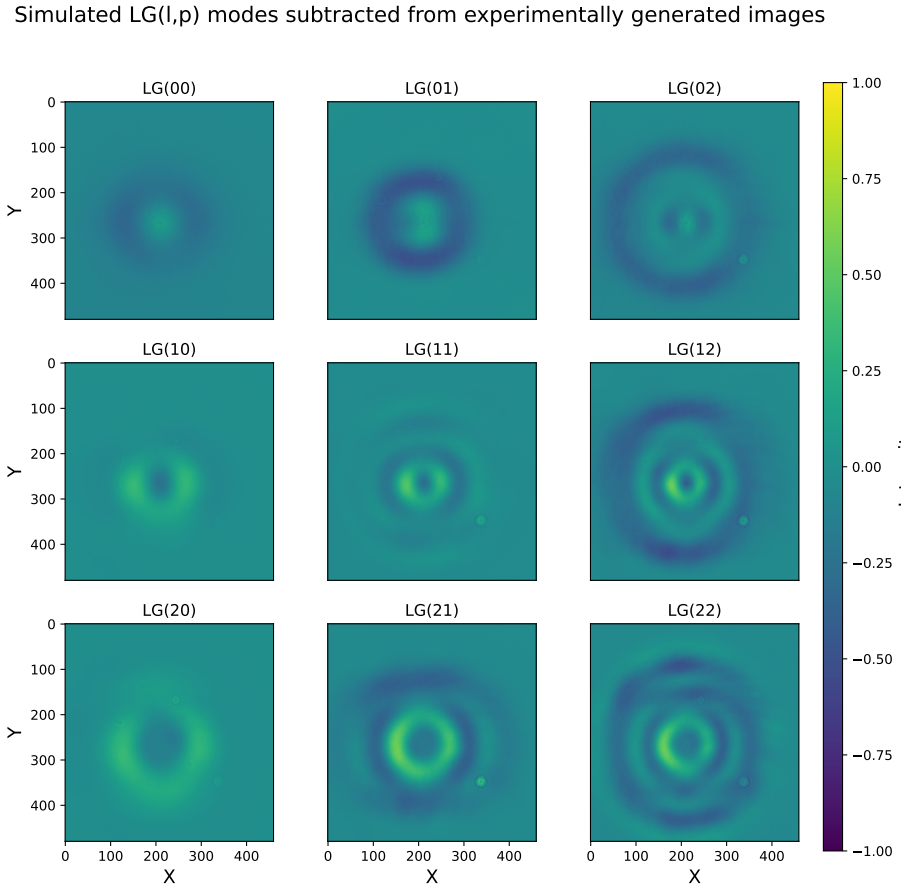

Figure 4.17: Subtracted intensity of simulated and detected LG modes

mode has a homogeneous intensity for all angles. For the images taken in the experiment, it is clear that a higher intensity is located above and below the center of the beam. Hence, a larger difference of the two images can be seen left and right of the center.

For a better comparison, the coefficient of determination R^2 can be taken into account, which is defined by

$$R^2 = 1 - \frac{\sum_{i=1}^{n}(X_i - Y_i)^2}{\sum_{i=1}^{n}(\overline{Y} - Y_i)^2}\,, \tag{4.10}$$

where n is the total number of events, X_i represents the predicted data, Y_i characterizes the experimental taken data and $\overline{Y}$ is its the mean value [48]. Its purpose is to characterize the correlation between the observed values and the theoretical ones. If the value for R^2 is zero, it implies that the two variables do not correspond well. If the value is close to one, we can conclude that the deviation from the theory is not severe [48]. For example the best correlations that can be obtained from this coefficient are a value of 0.922 for the LG(10) mode and 0.881 for LG(20). Some of the other LG modes show a higher

deviation from the theory for example LG(21) with a R^2 value of 0.559. It is concluded that we need further optimization methods to image them more precisely.

The quality of the produced LG beams can be compared to the quality of the HG modes created with the amplitude filter. The created HG modes are shown in Figure 4.15, and the difference between the experimentally obtained HG modes and the theoretical predictions is shown in Figure 4.18. It becomes obvious that there is less intensity left when subtracting the two images than there was for the LG modes. Hence, we assume that the captured images of the HG modes are closer to the expected ones. We have to deal with the same issues that were already discussed when describing the subtracted intensities for the other modes, for example some artifacts due to too much power exposure on the camera. The coefficient of determination can also be calculated for the HG modes. Here more modes show a result for R^2 that is close to a value of one, which implies that the captured images are close to the predicted ones. For example the mode HG(02) exhibits an R^2 value of 0.931.

It is concluded that the imaging of the HG modes led to better results. Implementing additional improvement methods might even lead to a better outcome, especially for higher modes.

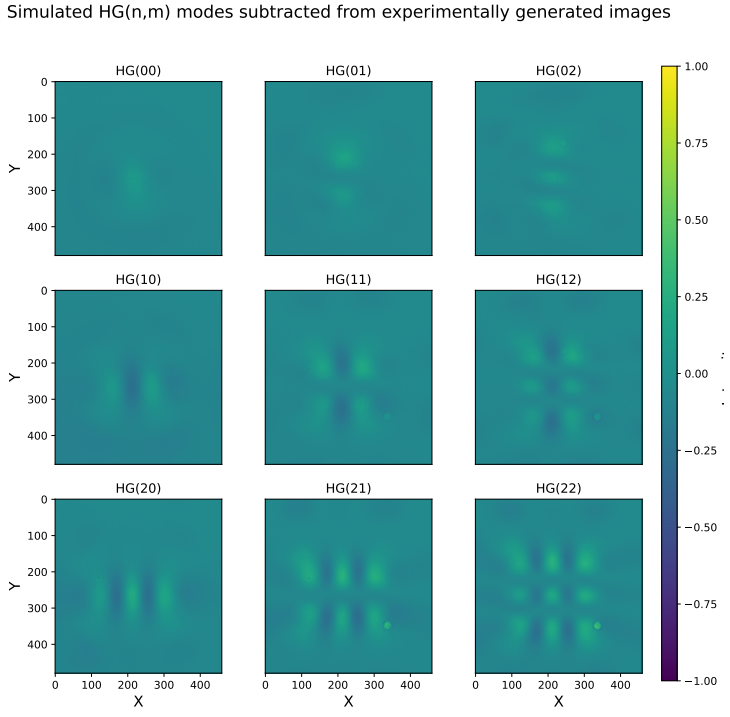

Figure 4.18: Subtracted intensity of simulated and detected HG modes

CHAPTER 5

Conclusion and Outlook

The aim of this thesis is to create and characterize non-Gaussian beams with a spatial light modulator. In the scope of this thesis, I therefore created different Laguerre Gaussian as well as Hermite Gaussian modes, detected them with a camera, and I tried to optimize the result.

First, a theoretical consideration of different beams was discussed. Here we started with the Maxwell equations known from classical electromagnetism to derive the wave equation as well as the Helmholtz equation. Different solutions of this equation like the Gaussian, HG and LG modes were derived, and their properties were discussed. The Gouy phase of these different beams was compared to the one of a Gaussian beam and we were able to see that a LG beam has an additional phase dependence of $\exp(il\phi)$ on the azimuthal angle, which implies that such a beam carries OAM. The fundamental properties of OAM were explained as well. This part of theoretical consideration was mandatory to understand how the phase masks are generated later.

Because the creation of the mentioned modes is aimed for in this thesis, the modulation of the phase of the light has to be investigated and therefore the SLM is taken into consideration. First its working principle was discussed to comprehend further measurements. Then I characterized important properties including how the phase modulation scales with the pixel values. To do this I used the SLM in a Pockels cell configuration where I modified the phase of one polarization direction. The contrast accomplished with this setup was $\eta = (0.955 \pm 0.017)$, which is a satisfying outcome. The intensity will not reduce completely to zero due to for example light sources coming from other experimental setups in the same laboratory. From the same data we obtain that a 2π phase modulation is accomplished after an input signal of (202 ± 2) instead of the specified value of 206 by the manufacturer. The difference between the two values is possibly caused by a too large angle of incidence of the initial setup. If the angle of incidence is greater than zero, the pixels of the SLM cannot be assumed to be quadratic anymore. Later the angle was reduced to minimize this effect.

The SLM provides a correction pattern for the phase front. But the application of this leads to a loss of contrast, indicating that the wavefront settings are not necessarily perfect for the SLM. Applying the WF as well as the LUT setting leads to an accomplished 2π modulation at a higher input signal level of (254 ± 2). The contrast decreased to a value of $\eta = (0.728 \pm 0.405)$. Because of unexpected curve behavior and a reduced contrast those options were not used for further measurements.

After characterizing the SLM, the holograms to modulate the phase of the laser beam were discussed. For the ability to image them I build a set for experimental creation of the modes. The taken images of various LG and HG modes are shown. Because of the low resolution the waist sizes cannot be calculated. Unfortunately, a lot of aberrations occur. An additional amplitude mask is imposed onto the phase mask with the aim to only deflect the desired part of the beam into the first order of diffraction. We can notice that the imaged modes improved in size, shape and intensity distribution. Finally, the improved beams were compared to the theoretical modes derived in chapter 2. This comparison reveals that further optimization is necessary in particular for the LG modes.

Further optimization might be realized by numerically implementing the inverse sinc function mentioned in section 4.4. While performing the measurement it could also be seen, that the quality of the portrayed images was strongly influenced by the position of the concave lens of the second telescope. It might be worth to adjust it further or to use a single lens again. For that, the setup needs to be rearranged.

This thesis serves as a first step towards investigations of how strong effective interactions between single photon mediated by a quantum nonlinear medium leads to a modification of the photon propagation mode. To do this, the span of the $\vec{k}$ vector space must be replaced. To accomplish that, one ideally uses two SLMs, one before the ultracold atoms, and one after them. The first SLM could maybe make use of a phase mask of a LG mode created in this thesis. The other SLM would need a phase mask that is able to create a Gaussian beam from an initial for example LG beam. The next step could be to implement such a 'recovery' phase mask.

APPENDIX A

Additional information

Figure A.1 shows the geometry of the diffraction used to derive the Fresnel and Fraunhofer diffraction integral.

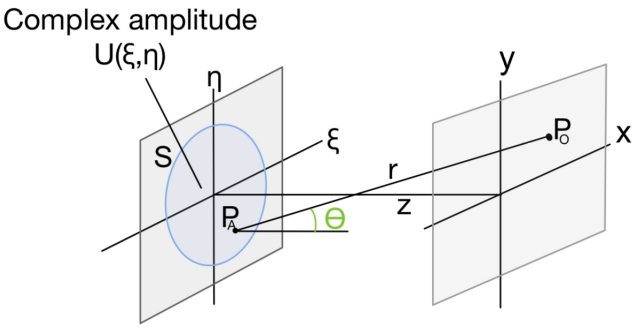

Figure A.1: Diffraction geometry, the complex amplitude distribution $U(\xi, \eta)$ propagates from aperture S towards the positive z-direction.The wave at point P_O results from the superposition of all the contributions of $U(\xi, \eta)$. (Based on image in [25].)

In Table A.1 we can see the fitting parameters for the phase modulation for different settings of the SLM. It is also shown for what input signal the 2π modulation is accomplished.

Table A.1: Fit parameters for phase modulation curves taken for different settings (see Figure 3.5, Figure 3.7, Figure 3.9 and Figure 3.10)

	LUT and WF off	WF on, LUT off	LUT on, WF off	LUT and WF on
a	0.981 ± 0.013	0.792 ± 0.044	1.0025 ± 0.0089	0.8434 ± 0.0062
b	$(1.8 \pm 8.1) \cdot 10^{-3}$	0.229 ± 0.029	$(1.47 \pm 0.53) \cdot 10^{-2}$	0.1468 ± 0.0039
c / 10^{-2}	(-3.067 ± 0.015)	(2.715 ± 0.084)	(2.345 ± 0.024)	(2.4606 ± 0.0086)
d	3.068 ± 0.012	-0.479 ± 0.063	0.128 ± 0.015	-0.6345 ± 0.0068
2π modulation	201.4 ± 1.8	252.6 ± 3.8	245.6 ± 4.8	253.6 ± 1.5

In Figure A.2 we can see the implemented phase masks for various HG modes.

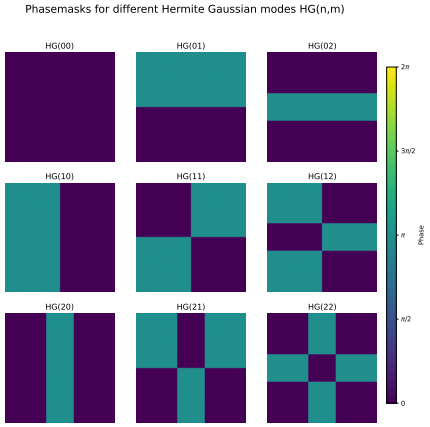

Figure A.2: Phase masks for different Hermite Gaussian modes

Figure A.3 shows the phase masks for multiple LG and HG modes for when a blazed grating is added, to observe the desired mode into the first order of diffraction.

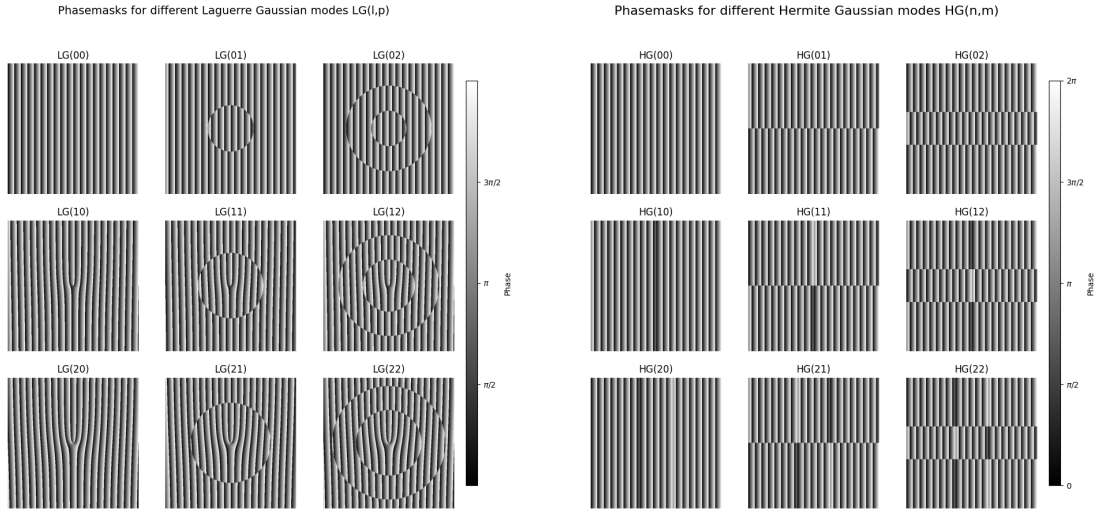

Figure A.3: Phase masks for different Laguerre-Gaussian (left) and Hermite Gaussian modes with blazed grating (right)

In Figure A.4 the horizontal and vertical waist sizes of a laser beam for different positions relative to the out coupling lens after the fiber is shown. A linear fitting function was used

$$f(x) = a \cdot x + b \ . \tag{A.1}$$

Based on the fit we obtain the following parameters for the vertical (v) and horizontal (h) direction:

$$a_{\mathrm{v}} = (3.27 \pm 1.99) \cdot 10^{-4} \qquad a_{\mathrm{h}} = (4.55 \pm 1.12) \cdot 10^{-4}$$
$$b_{\mathrm{v}} = (1.045 \pm 0.073)\mathrm{mm} \qquad b_{\mathrm{h}} = (0.908 \pm 0.037)\mathrm{mm}$$

Due to the small value for the slope we can assume that the beam is sufficiently collimated for the purpose of this work.

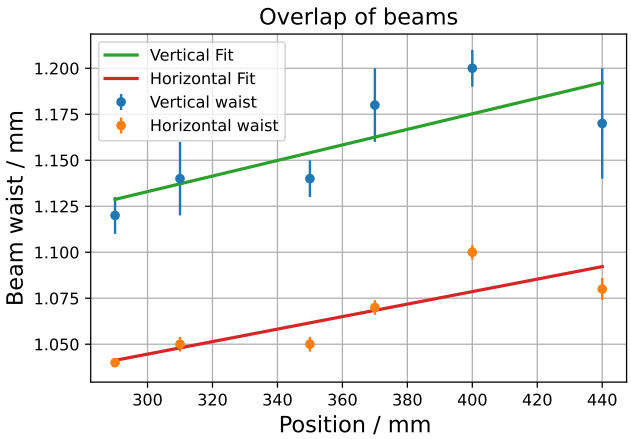

Figure A.4: Horizontal and Vertical Waists for beam at different positions relative to outcoupling lens

Figure A.5 shows the phase masks for HG modes where the presented optimization method is applied.

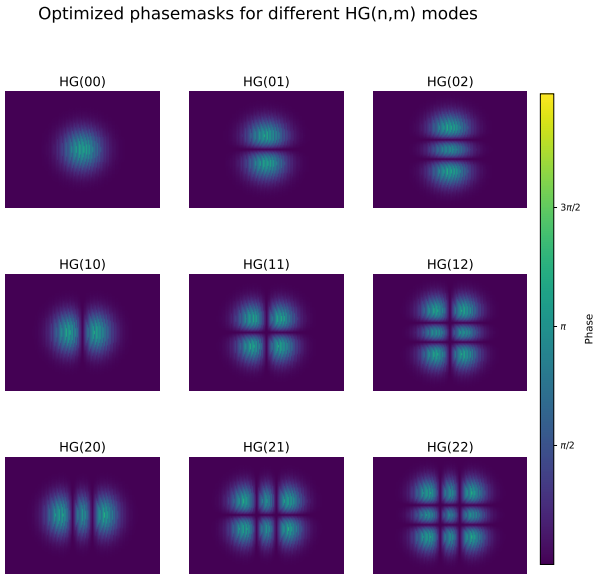

Figure A.5: Optimization of the phase masks for different HG modes

Bibliography

[1] F. Dietrich et al., *Laser cooling to the zero-point energy of motion*, Phys. Rev. Lett. **62** (1989) (cit. on p. 1).

[2] K. Davis et al., *Bose-Einstein condensation in a gas of sodium atoms*, Phys. Rev. Lett. **75** (1995) (cit. on p. 1).

[3] Sonja Franke-Arnold, *Optical angula momentum and atoms*, Phil. Trans. R. Soc. **375** (2017) (cit. on p. 1).

[4] O. Firstenberg, C. S. Adams and S. Hofferberth,
Nonlinear quantum optics mediated by Rydberg interactions,
Journal of Physics B: Atomic, Molecular and Optical Physics **49** (2016) 152003,
URL: https://dx.doi.org/10.1088/0953-4075/49/15/152003 (cit. on p. 1).

[5] Jan Kumlin et al., *Quantum Optics with Rydberg Superatoms*,
Journal of Physics Communications (2023) (cit. on p. 1).

[6] A. Faßbender, S. Linden et al.,
Direct phase mapping of broadband Laguerre-Gaussian metasurfaces,
APL PHOTONICS **3** (2018) (cit. on p. 2).

[7] Huanlu Li and David B. Phillip et al.,
Orbital angular momentum vertical-cavity surface-emitting lasers, Optica **2** (2015) 547,
URL: https://opg.optica.org/optica/abstract.cfm?URI=optica-2-6-547
(cit. on p. 2).

[8] B. Lee, *Introduction to ±12 Degree Orthogonal Digital Micromirror Devices (DMDs)*,
URL: https://www.ti.com/lit/an/dlpa008b/dlpa008b.pdf?ts=1713172229835&ref_url=https%253A%252F%252Fwww.google.com%252F (visited on 28/04/2024)
(cit. on pp. 2, 11).

[9] J. Clerk Maxwell, *A Dynamical Theory of the Electromagnetic field*,
Philosophical Transactions of the Royal Society of London **155** (1864) (cit. on p. 3).

[10] B. Saleh, *Fundamentals of Photonics*, Wiley, 2007 (cit. on pp. 3–5, 7, 8).

[11] J. W. Goodman, *Introduction to Fourier Optics*, Roberts Company Puplisher, 2005
(cit. on pp. 3, 13–15).

[12] E. Weisstein, *Paraxial Approximation*,
URL: https://scienceworld.wolfram.com/physics/ParaxialApproximation.html
(visited on 17/04/2024) (cit. on p. 4).

[13] Richard Rasala, *The Rodrigues Formula and Polynomial Differential Operators*, Journal of mathematical analysis and applications **84** (1981) (cit. on pp. 7, 8).

[14] *HermiteGaussianBeam*, URL: https://jcmwave.com/docs/ParameterReference/0a2dd5b44fc46b68bd3c44031b2aecd4.html?version=4.4.0#hermitegaussianbeam (visited on 25/04/2024) (cit. on p. 7).

[15] Hyo-Chang Kim et al., *Hermite–Gaussian and Laguerre–Gaussian beams beyond the paraxial approximation*, Phys. Rev. A **11** (1975), URL: https://www.sciencedirect.com/science/article/pii/S0030401899004113?ref=pdf_download&fr=RR-2&rr=879ee21e298fbb49 (cit. on pp. 7, 9).

[16] G. Vallone, *On the properties of Circular-Beams: normalization, Laguerre-Gauss expansion and free-space divergence*, Opt Lett. (2015) 1717, URL: https://arxiv.org/pdf/1501.07062.pdf (cit. on p. 8).

[17] Alison M. Yao et al., *Orbital angular momentum: origins, behavior and applications*, Advances in Optics and Photonics **3** (2011) (cit. on pp. 9, 10).

[18] L. Stoyanov et al., *Optical vortices in brief: introduction for experimentalists*, Eur. Phys. J. Plus **138** (2023) 702 (cit. on p. 9).

[19] A. E. Willner, *Twisted Light Could Dramatically Boost Data Rates*, URL: https://spectrum.ieee.org/twisted-light-could-dramatically-boost-data-rates (visited on 01/05/2024) (cit. on p. 9).

[20] L. Allen et al., *Orbital angular momentum of light and the transformation of Laguerre-Gaussian laser modes*, Phys. Rev. A **45** (11 1992) 8185, URL: https://link.aps.org/doi/10.1103/PhysRevA.45.8185 (cit. on p. 10).

[21] *Spiral Phase Plate*, URL: https://www.holoor.co.il/product/spiral-phase-plate-vortex/ (visited on 28/04/2024) (cit. on p. 11).

[22] Aurélie Jullien, *SPATIAL LIGHT MODULATORS*, Photoniques **101** (2020) (cit. on p. 11).

[23] Hamamatsu, *Principle LCOS-SLM (optical phase modulator)*, URL: https://www.hamamatsu.com/jp/en/product/optical-components/lcos-slm/priciple.html (visited on 11/04/2024) (cit. on pp. 11, 12).

[24] Holoeye, *Spatial Light Modulators*, URL: https://holoeye.com/products/spatial-light-modulators/ (visited on 11/04/2024) (cit. on p. 12).

[25] G. Dijk, *Intensity Patterns Generated with a Spatial Light Modulator*, Technische Universität Eindhoven, 2012, URL: https://arxiv.org/pdf/1303.4496.pdf (cit. on pp. 12, 13, 44).

[26] J. Pan et al., *Far-field radiation estimation from near-field measurements and image theory*, 2014 IEEE International Symposium on Electromagnetic Compatibility (EMC) (2014) (cit. on p. 13).

[27] *LCOS-SLM Operation manual*, H, Hamamatsu, 2018 (cit. on pp. 15, 17, 20–23, 26).

[28] J. A. de Haan, *Holographic Generation of Arbitrary Intensity Patterns*, Rheiniche Friedrich-Wilhelms-Universität Bonn, 2022 (cit. on pp. 15, 26).

[29] H. Asaine, *Final inspection sheet*, Hamamatsu, 2017 (cit. on pp. 16, 20, 23).

[30] Spie, *Jones Calculus*, URL: https://spie.org/publications/spie-publication-resources/optipedia-free-optics-information/fg05_p57-61_jones_matrix_calculus?SSO=1 (visited on 16/04/2024) (cit. on pp. 16, 17).

[31] G. F. Torres del Castillo et al., *The Jones vector as a spinor and its representation on the Poincaré sphere*, Rev. Mex. Fis. **57** (2013) 406, arXiv: 1303.4496 (cit. on p. 17).

[32] Richard Neo et al., *Use of the poincare sphere in polarization optics and quantum mechanics*, Review Radiophys Quantum Electron **40** (1997) 175 (cit. on p. 17).

[33] Thorlabs, *Digital Handheld Optical Power and Energy Meter Console*, URL: https://www.thorlabs.com/newgrouppage9.cfm?objectgroup_id=3341 (visited on 19/04/2024) (cit. on pp. 19, 28).

[34] Eli Peli, *Contrast in complex images*, J. Opt. Soc. Am. **7** (1990) 2032 (cit. on p. 19).

[35] *LCOS-SLM Software operation manual*, D, Hamamatsu, 2016 (cit. on pp. 20, 21).

[36] Alicia V. Carpentier et al., *Making optical vortices with computer-generated holograms*, American Journal of Physics **76** (2008) (cit. on p. 25).

[37] L. Janicijevic, *Fresnel and Fraunhofer diffraction of a Gaussian laser beam by fork-shaped gratings*, J. Opt. Soc. Am. A **25** (2008) 2659 (cit. on p. 26).

[38] Vitawave, *Technical description and instruction manual of an extended cavity diode laser ECDL-7830R (S/N 121111)*, URL: https://wiki.nqo.uni-bonn.de/images/ECDL-7830R_121111_Vitaly.pdf (visited on 19/04/2024) (cit. on pp. 26, 27).

[39] Thorlabs, *Optical Isolator Tutorial*, URL: https://www.thorlabs.de/catalogPages/680.pdf (visited on 19/04/2024) (cit. on p. 26).

[40] Unibrain, *Unibrain Ultra Compact firewire camera - User Operation Manual*, URL: https://wiki.nqo.uni-bonn.de/images/Unibrain_Fire-i_530.pdf (visited on 25/04/2024) (cit. on p. 27).

[41] *MT9J003 1/2.3-Inch 10 Mp CMOS Digital Image Senso*, URL: https://wiki.nqo.uni-bonn.de/images/MT9J003-D.PDF (visited on 03/05/2024) (cit. on p. 27).

[42] W. Demtröder, *Experimentalphysik 1 - Mechanik und Wärme*, 7th ed., 2015 (cit. on p. 28).

[43] *FIBER SPECIFICATIONS*,
URL: https://www.thorlabs.com/drawings/b415fcb8ff7efe2d-DA9E257A-0C52-FBF7-A3D51509A04CCDC9/P3-780PMP-2-AutoCADPDF.pdf (visited on 30/04/2024)
(cit. on p. 28).

[44] sourceforge, *GaussianBeam*,
URL: https://gaussianbeam.sourceforge.net/ (visited on 25/04/2024)
(cit. on pp. 28, 29).

[45] R. M. W. van Bijnen, *Quantum Engineering with Ultracold Atoms*,
University of Technology Eindhoven, 2013 (cit. on p. 28).

[46] E. Bolduc et al.,
Exact solution to simultaneous intensity and phase encryption with a single phase-only hologram,
OPTICS LETTERS **38** (18 2013) 3546 (cit. on pp. 33, 34).

[47] J. A. Davis et al., *Encoding amplitude information onto phase-only filters*,
Appl. Opt. **38** (1999) 5004 (cit. on p. 34).

[48] D. Chicco et al., *The coefficient of determination R-squared is more informative than SMAPE, MAE, MAPE, MSE and RMSE in regression analysis evaluation*, PeerJ Comput Sci. (2021)
(cit. on p. 40).

Acknowledgements

I would like to thank the whole NQO group for an amazing time. I was able to learn so many new things within just four months and I am really thankful for it.
I would like to thank Prof. Sebastian Hofferberth for giving me the opportunity to write my Bachelor thesis in his group on this interesting topic.
Thank you to Prof. Stefan Linden, who is the second corrector of my thesis.
Especially I would like to thank Daniil, who did an amazing job supervising me and invested a lot of time into this project.
Thank you to Nina, who was always there for me whenever I had questions and had so many nice ideas regarding this project.
I would also like to thank Lukas and Jan, who explained many things in the lab to me even when they were busy sometimes.
Thanks to Hannah, who always tried to solve problems with me and who has been the best lab mate, which contributed to a really funny time that sometimes even led to tears from laughing too much.
Thank you Theresa for being an amazing friend, always giving me advice and completing the eingespieltes trio.
Thanks Julia for a lot of coffee and tea breaks that were always a joy.
Thanks to Ludwig, who was always in a good mood.
Thank you to Tina, who was always super kind and organized everything.
And also a big thank you to the rest of the group. It was an amazing time for me and I am really glad that I got to meet every single one of you.
Finally, I would like to thank my family, friends and my flat mates, who always supported me.